Segregation in binary and polydisperse stirred media mills and its role on grinding effectiveness

Rhymer, D.; Ingram, A.; Sadler, K.; Windows-Yule, C.R.K.

DOI:
10.1016/j.powtec.2024.119921

Journal Pre-proof

Segregation in binary and polydisperse stirred media mills and its role on grinding effectiveness

D. Rhymer, A. Ingram, K. Sadler, C.R.K. Windows-Yule

PII: S0032-5910(24)00564-3
DOI: https://doi.org/10.1016/j.powtec.2024.119921
Reference: PTEC 119921

To appear in: *Powder Technology*

Received date : 25 January 2024
Revised date : 3 May 2024
Accepted date : 22 May 2024

Please cite this article as: D. Rhymer, A. Ingram, K. Sadler et al., Segregation in binary and polydisperse stirred media mills and its role on grinding effectiveness, *Powder Technology* (2024), doi: https://doi.org/10.1016/j.powtec.2024.119921.

Segregation in binary and polydisperse stirred media mills and its role on grinding effectiveness

D. Rhymer[a,*], A. Ingram[a], K. Sadler[b], C. R. K. Windows-Yule[a]

[a]*School of Chemical Engineering, University of Birmingham, Edgbaston, Birmingham, B15 2TT, UK*
[b]*R&D Mondelez International, Bournville, Birmingham, B30 2LU*

Abstract

Most industrial **vertical** stirred mills contain a non-uniform set of grinding media sizes. However, this fact is often ignored in simulations, which mostly use monodispersed media. The paper explores the **fundamental dynamics of vertical mills when using multiple sizes of grinding media**, by using DEM simulation. Our results suggest that by including both large and small media, one may be able to optimise its performance in several manners. **The energy going into the contacts can be increased by including a second size, leading to more effective grinding.** Including smaller media can also reduce the power draw of the mill, increasing the efficiency and sustainability of the mill. **Finally, the natural segregation between different sizes creates different types of collision which grind different particle sizes more effectively**. Segregation leads to smaller media at the bottom, so continuous processes can be optimised for fine grinding by feeding from the top, where the larger media are. This further enables control of the resulting product specifications.

*dcr502@bham.ac.uk

Keywords: Vertical Stirred Mill, Discrete Element Method (DEM), **Grinding Media Polydispersity**, **Segregation Effects**, **Grinding and Comminution**, **Power Draw**

1. Introduction

Within industrial stirred mills, almost no system has a full set of identically sized grinding media [1]. There are several reasons for this. The most common is due to manufacturing, but the differences are also caused by ageing and wear, **particularly in continuous mills which are becoming increasingly common in almost every industry [1–5]. de Bakker [1], even stated that one of the most common errors in research is using monodisperse media, which will give a higher specific energy than reality.** Because of the nature of the technique, media become smaller over time until they pass out of the mill naturally. **The lost material is replenished periodically to maintain overall media mass. Altun *et al.* [6] investigated the effects of media wear on an industrial and laboratory scale mill, observing noticeable differences in the amount of wear caused by using different materials.** Mill operators may also deliberately choose to use multiple media sizes because they have different benefits on the grinding performance [4, 7, 8]. Smaller media produce a finer grind as stated by Napier-Munn *et al.* [9], and later Edwards [10] because their increased collective surface area benefits finer grinding. However, Jankovic [11] did state that there may be a deterioration in mill efficiency below a certain size limit, presumably because there becomes insufficient energy within smaller media. [9].

Previous studies compare the milling performance of different media sizes [12]. Mankosa, Adel and Yoon [13] were one of the first groups to do this by investigating the effects of media size within a low-speed stirred mill (200-330 rpm). They concluded that the optimal ball size to particle feed size ratio was 20:1 and although this was for dry coal, their conclusions still hold for most conditions including slurries. Blecher *et al.* [14] subsequently demonstrated that smaller grinding media were more likely to follow streamlines in the mill and, therefore, were more likely to influence grinding performance. Meanwhile Kwade, Blecher and Schwedes [15] suggested that using different media sizes within the same mill would be beneficial as larger media sizes produced a finer grind at lower specific energies and smaller media sizes were more effective at higher energies. Bel Fadhel and Frances [16] later agreed with these conclusions [10].

A recent review article by Kumar, Sahu and Tripathy [17] highlights this by mentioning that media size distribution has an effect on grinding but not citing any studies which investigate the effects of having multiple size fractions present. Sinnott, Cleary and Morrison [18] did investigate the effects of a polydisperse size range but only for a single media charge as part of a wider shape study. Jayasundara, Yang and Yu [19] investigated the effects of using different media sizes in a horizontal mill computationally, but each charge was a single size. This is just one example of a series of studies that have observed the effects of different-sized media within horizontal setups [20–24]. Cho *et al.* [8] took this one step further by comparing a monodispersed experimental mill with simulated binary and three-size bead distribution ratios. They concluded that a binary system of the largest and smallest size was optimal, rather than including an additional intermediate size. More recently, Soni and Mishra [25], and then Yari *et al.* [26] have simulated at least binary dispersity in a tumbling mill particle distribution. While the former based their study around mill speed and concluded that there was an optimum for reducing segregation, the latter focused on the size ratio, finding that different regimes occurred at different ratios. **While there is a lack of findings which highlight the effects of having multiple particle sizes, literature discusses segregation phenomena and theory in other processes [27–33], so the effects can be compared to those found within the vertical mill.**

While there has been significant research into the effect of particle size in monodisperse systems [12–15], there has, to date, been no detailed, systematic study of the behaviour of Vertical Stirred Mills containing binary or polydisperse media charges. This study aims to address this gap by investigating:

- **The effects of having two sizes of media within a Vertical Stirred Mill.**
- **How changing the size ratio of two fractions affects grinding performance.**
- **How changing proportions of large and small media affects performance.**

Simplifying the case to binary size distributions initially allows for deeper exploration and more definitive identification of the effects caused by different ratios compared to using a full polydispersed distribution. **While grinding**

would affect shape and surface properties which are highly important in industry too, this approach isolates the effect of size specifically and focuses on key findings. A few polydispersed simulations were run towards the end of the study to see if observations were consistent across more complex media size distributions.

2. Methodology

2.1. DEM contact model

DEM is based on Cundall and Strack's original description of the interaction between two particles in contact [34]. Two equations, defining the translational (Equation 1) and rotational (Equation 2) velocities, can be derived from the resultant forces and torques shown in Figure 1 [34–36].

$$m_i \cdot \frac{dv_i}{dt} = \sum (F_{ij}^n + F_{ij}^t) + m_i \cdot g, \tag{1}$$

$$I_i \cdot \frac{d\omega_i}{dt} = \sum (R_i \cdot F_{ij}^t - \tau_{ij}^t), \tag{2}$$

where F_{ij}^n and F_{ij}^t are the normal and tangential components of force, and m_i, v_i, I_i, ω_i and τ_{ij}^t represent the particle mass, translational velocity, moment of inertia, rotational velocity and rolling friction. R_i is the distance between the particle centre and the tangential contact point and g is the gravitational force [35–38].

LIGGGHTS® (LIGGGHTS v3.8.0, DCS Computing GmbH, Austria) [39], an open-source DEM package, was used to carry out the simulations. The model used was the Hertz-Mindlin no-slip method, and this defines the normal and tangential forces of a single pair of particles in contact (Equations 3 and 4 respectively) [40].

$$F_{ij}^{n} = K^{n} \cdot \delta_{ij}^{n} - \gamma^{n} \cdot v_{ij}^{n}, \tag{3}$$

$$F_{ij}^{t} = K^{t} \cdot \delta_{ij}^{t} - \gamma^{t} \cdot v_{ij}^{t}. \tag{4}$$

Each equation is the sum of an elastic and dissipative component. K^n and δ_{ij}^n are the elastic constant and normal particle overlap and $\gamma^n \cdot v_{ij}^n$ is the normal dissipative force. The equivalent tangential terms, K^t, δ_{ij}^t and $\gamma^t v_{ij}^t$ are used in Equation 4. K^n and K^t can be calculated from input data and $\gamma^t v_{ij}^n$ [38]. A full derivation can be found in Appendix A [40].

2.2. Model setup

A template model was created and validated based on the previous experimental results of Rydin *et al.* [41] and simulation work of Daraio *et al.* [36]. In the spirit of open and transparent science, the base model used for this work has been made freely available at https://github.com/darhyme147/liggghts_stirred_mill_template **such that other researchers may independently reproduce and verify our results, and more generally benefit from the use of this calibrated model in their work. For direct comparison, and validation, with the experimental data reported by Rydin et al [41], their geometry was reproduced and the simulation focussed on** 10 mm **media at attritor speeds of** 50 **and** 250 rpm (0.43 **and** 2.17 m s^{-1} **tip**

speed). While the tip speed could be considered low for some applications, in the context of food, this is a reasonable range that agrees with previous studies [2, 42]. The geometry, shown in Figure 2, and the remaining parameters reproduce the long arms design from Daraio *et al.* and are shown in Table 2. The mill contained $14.80\,\mathrm{kg}$ of media ($55\,\%$ fill level) [36] which were modelled with the properties of stainless steel. A restitution coefficient of 0.7 and sliding friction of 0.25 were also selected from the previous work [36, 43], while the rolling friction was set to zero; a reasonable assumption for spherical media particles considered here [44, 45]. The validation results are shown in Section 4.

Five simulation batches were run, each defined by the ratio of the two media diameters. The larger size was fixed at $10\,\mathrm{mm}$, while the smaller varied between $2.5\,\mathrm{mm}$ and $7.5\,\mathrm{mm}$. A timestep of $10^{-6}\,\mathrm{s}$ was selected as this is 140 times smaller than the critical timestep obtained for the $2.5\,\mathrm{mm}$, using the Equation proposed by Thornton and Randall (Equation 5) [36, 46],

$$t_{cr} = \frac{\pi \cdot R \cdot \sqrt{\rho/G}}{0.01631 \cdot \nu + 0.8766}. \quad (5)$$

ρ is the particle density and G is the shear modulus. The numerical proportion of the two media size fractions was also changed while maintaining the overall mass. With five size ratios, eleven proportions and five attritor speeds, a total of 275 simulations were performed and analysed. Each was run on a high-performance cluster using 4 cores of an Intel® Xeon® Platinum 8360Y CPU

processor [47].

2.3. Post-processing

2.3.1. Media segregation

Because a binary-size distribution was used, media segregation will be present. Segregation is a phenomenon whereby particles of different properties, in this case, size, fully or partially separate into individual fractions [32]. Any physical property difference can cause segregation, including size [25, 26, 48], density [28, 31], geometry [49], and surface properties [27]. Mixing indexes are one way of quantifying segregation and the Lacey mixing index has been used in this study (Equation 6). To calculate this, the milling region is divided into equal volume cells [50, 51],

$$M = \frac{\sigma_0^2 - \sigma^2}{\sigma_0^2 - \sigma_r^2}. \tag{6}$$

σ^2 is the variance of the concentration of a reference component within each cell of the system in question and can be expressed using Equation 7,

$$\sigma^2 = \sum_{i=1}^{N} \frac{(\phi_i - \phi_m)^2}{N-1}, \tag{7}$$

where N represents the number of cells occupied by media, ϕ_i is the local concentration of the reference component in cell i and ϕ_m is the global concentration of the reference component. For a binary system, like the ones observed here, the maximum variance, σ_0, can be determined as

$$\sigma_0^2 = \phi_m(1 - \phi_m). \tag{8}$$

Finally, the theoretical minimum variance of a cell, σ_r is defined by

$$\sigma_r^2 = \frac{\phi_m(1-\phi_m)}{n}, \tag{9}$$

with n being the maximum number of particles that can fit within an individual cell.

2.3.2. Collision kinetics

When grinding, the aim is to maximise the number of successful media collisions. An ideal system will be able to reach the desired particle size distribution for the minimum energy input. Therefore, the best way to increase the number of successful collisions is to increase the probability of a successful collision happening; either by increasing contact frequency or by increasing the average contact energy.

As each simulation was sampled, an approximation for collision frequency is defined as an average of the total number of contacts present per second. **In a binary size distribution, there are three types of contact present: contact between two beads of the larger media size, between two beads of the smaller size, or between one larger and one smaller sized bead. This has been quantified for each simulation.** As well as frequency, the magnitude and type of collision can be quantified. Beinert *et al.* [52] proposed that a pair of spherical beads in contact would exhibit at least one of six main collision mechanisms, shown diagrammatically in Figure 3. Table 1 shows the associated Equations that can be derived from each of these mechanisms. A more detailed explanation can be found in Rhymer *et al.* [40]. The total energy of collision, E_{total}, is the sum of all six components.

2.3.3. Power draw

As the mill was studied at steady state conditions, instantaneous power draw can be found from the summation of all dissipative energies. Most of this energy is media-media collisions, and individual collision values can be found by multiplying the dissipative force components from Equations 3 and 4 by the corresponding relative pair velocity (normal and tangential). There are also media-wall collisions and these are calculated similarly. In LIGGGHTS, the relative collision velocity can be found using two methods; either through direct calculation of the damping coefficient, γ, or by using the output data provided to find $\gamma \cdot v$ and then taking the difference between the total and elastic component. This latter method was preferred because it is based on output data rather than inputs, meaning any additional damping assumptions LIGGGHTS uses during simulation to maintain model stability are factored into the overall result.

Design equations for power draw within mills also exist. Kwade *et al.* [15] derived a stress model from their studies of different media within a horizontal mill. This was later used by Radziszewski and Allen [53, 54] to create a simple correlation for power that relies on the rotational velocity, ω, perceived dynamic viscosity, η, and shear volume, V_τ,

$$P = \eta \omega^2 V_\tau. \tag{10}$$

η is estimated from Gao, Forssberg and Weller's correlations [55]. V_τ is a sum of all of the surfaces undergoing shear, I, (Equation 11), with A being the area undergoing shear, r_s, the radius that the shear is acting, and y, the separation between surfaces,

$$V_\tau = \sum^{I} A \frac{r_s^2}{y}, \tag{11}$$

The Equation proposed by Radziszewski and Allen is very difficult to validate accurately, especially within simulation. η can only be determined through experimental work, and contains several terms to account for the many different parameters within the mill. V_τ is also complex to accurately determine as the shear volume can change with rotational velocity. A vortex develops in the centre of the mill, meaning some of the shear surfaces lose contact with the slurry. The previous paper with Osborne [56], also suggested that the surfaces between pins needed to be included in the shear volume to be more robust for a greater number of designs.

3. Results and Discussion

The results present time-averaged data for ten seconds of simulation, at 20 samples per second. This was once the mill had reached the correct velocity, and steady state (See Appendix B). The open-source tool Paraview [57] was used to check that the simulations had run properly and if there were any visual differences between different parameters. All visual images were further post-processed in Blender [58]. The LIGGGHTS data was numerically processed and analysed using Python.

3.1. Media segregation

As explained in Section 2.3.1, segregation effects are present due to having multiple media sizes. Figure 4 shows examples of this for the different size ratios. As the ratio increases, the rate of segregation and purity of the two layers increases; which is as expected from segregation theory of other engineering systems [25, 27, 59]. This is true at 50 rpm, (a)-(e), where the input energy from the attritor cannot create enough lift to overcome percolation effects, so the smaller media fall to the bottom of the mill naturally. At 250 rpm, these effects are still observed but with less effect as the attritor energy supplied is large enough to lift the smaller media into the larger ones. This is true in all sizes except 2.5 mm, Figure 4(j). There is an insufficient volume of smaller media to generate the height that would bring some into the path of the attritor, despite being 80% of the total media count. Industrially, this is significant because a large percolation effect and segregation could result in inefficient grinding if the direction of the slurry flow is incorrect. It has already been discussed that optimal grinding occurs when the bead-to-particle ratio is around 20:1 [13], meaning smaller media should produce a finer grind and should therefore be at the end of the slurry flow if possible for optimal comminution [9, 10]. This would lead to an ideal flow from top to bottom but could lead to channelling and other flow-related issues if not controlled correctly. As gravity would be drawing slurry downwards, residence time would also be reduced by doing this, so it would be necessary to introduce some level or flow control.

Figure 5 shows the azimuthally projected (r-z axis) volumetric bead distribution for different attritor speeds and size ratios. As in Figure 4, these were all for a 20% count of 10.0 mm media. Volumetric plots were used to provide representative spatial distributions inside the mill. These show the media segregated by the separation of the different colours. Interestingly, each plot shows a continu-

ous band of equal volume fraction (the white region). The region is larger at higher attritor speeds and smaller media size ratios. As the size ratio increases, this transition becomes smaller and the colours intensify, suggesting stronger segregation is present. At higher speeds, a vortex forms in the centre of the mill because of the increase in centrifugal force [15, 60, 61]. In some industrial cases where high impact is required, this is undesirable and baffling would be used to promote media chaos [53].

3.1.1. Lacey mixing index

While occupancy provides a qualitative view of segregation, a mixing index provides a quantitative evaluation. Figure 6 plots the Lacey mixing index for the equiproportional simulation for each size fraction and rotational speed. There is generally a negative correlation in the Lacey index as the size ratio increases. Within each line, there is a fluctuation due to noise from the instantaneous nature of the sampling, but otherwise, the values stay fairly consistent for each simulation. The indices for the 3.75 mm are much lower than the rest of the size ratios, especially at low attritor speed. This indicates that the percolation effect is significant enough for almost complete segregation. However, as the attritor velocity increases, the smaller fractions are lifted by the attritor, creating enough re-circulation to at least partly overcome the segregation effects.

A time-averaged value for Lacey can also be calculated and plotted by media count proportion for each simulation (Figure 7). In agreement with Figure 6, these show that the larger the size ratio, the lower the index value, which concurs with previous segregation theory [59]. The value is also highest when the proportion of 10 mm beads is around 30-40%, though the exact proportionality depends on the size ratio between the two media sizes. This might be because they are closer to equivolume; something which appears to have a greater influence than numeric quantity. While most curves are concave in nature, higher size ratios at low attritor velocities are convex to the abscissa. Industrially, these plots show that uncontrolled size distributions could become a big concern if there are large effects from having multiple sizes as hypothesised. It also potentially reveals that there are limits in size ratio, proportionality, attritor speed and system design that will cause poor re-circulation and will want to be avoided when optimising milling equipment.

3.2. Media velocity

The average velocity versus 10 mm volume fraction is shown in Figure 8. Each subplot shows the results for a different size ratio. A greater proportion of 10 mm beads leads to greater velocities. The reason is that contact dissipates energy, so with smaller beads, there are more contacts dissipating energy. More of the media can also fit in the dead region previously described. There is an approximately linear relationship between attritor speed and media velocity. That linearity agrees with the results of previous work [40], because the tip speed of the attritor changes linearly for the selected rotational speeds. As large amounts of smaller media are introduced, the velocity further decreases. As with the changes by proportion, the trend can be described through the additional dissipation of the extra contacts within the mill. At higher attritor speeds, there is media separation because of the centrifugal force generated which also contributes to loss of contact between media.

Velocity field maps have been generated to show the 2-D behaviour of the mill (Figure 9). Each simulation presented had an attritor speed of 250 rpm. If the mill is exclusively comprised of small media, Figure 9(a), the volume of the highest velocity is larger when the media are bigger. This goes back to the principles of fewer media contacts so less energy is dissipated. As the size starts to decrease, the regions of the highest velocity are raised towards the upper pins, with less velocity lower down. The tighter packing leads to more collisions and a faster dissipation rate.

When media count is equiproportional, (b), there is a counteracting effect, with a smaller second diameter providing greater average velocity in the central milling area. This is because of the segregation effect, meaning if the second media size is small, the area between the pins is almost all 10 mm media. When 7.5 mm media are included, there is a large enough volume and slow enough segregation rate to mean that some media get stuck within the pin region and create extra collisions. However, this is not the case when 3.75 mm media are the smaller fraction. The size ratio means that the smaller media percolate and gather at the bottom, meaning the high energy regions are almost exclusively 10 mm media.

3.3. Media force

While velocity has a non-linear correlation with media proportion, the average media force shows linearity, especially when considered by count proportion. Figure 10 shows the average media force plotted against proportion for different size ratios. These plots show that as the proportion of 10 mm beads increases, the net force on each media bead also increases [4, 19]. This is expected as larger media carry larger mass providing density is kept constant. However, the fact that the distribution is linear when the average force is plotted against the count proportion is surprising. While it would be natural to assume a weighted proportion based on two individual media forces that stay reasonably constant, it would imply that there is a uniform behaviour throughout.

The linear plots in Figure 10 were combined and normalised by the tip speed to consider the effect of increased attritor velocity, shown in Figure 11. Each plane does not sit perfectly on one another, particularly as the proportion of 10 mm beads and smaller bead sizes increase. This aligns with the conclusions of previous work [40], which suggested that increased attritor velocity provides a greater average force per unit of input energy. In the case of different media sizes and proportions, the average media force increases with a greater proportion of large media. Again, this can be expected but there is less linearisation as media diameter changes. Here, there is a slightly exponential trend as media diameter increases, particularly at higher proportions of smaller media.

3.4. Contact energies

3.4.1. Energy distribution

Successful grinding depends on collisions between media particles containing sufficient energy to fracture any particulate material which could be trapped in between them. As one of the limitations of the simulation method is the ability to include any particulate material or breakage models, there needs to be some way of predicting the grinding potential. Linear distribution plots showing the spread of collision energies within the mill is one way of doing this. These generate a probability distribution of the likelihood of a successful collision. This data has been collated overall time outputs using the Beinert *et al.* [52] calculation method (See Section 2.3.2).

Figure 12 shows different energy distributions when 7.5 mm are the smaller media. As the attritor velocity increases from 50 rpm in (a), to 200 rpm in (d), the energy distribution shifts to the right, meaning that on average, each collision has more energy and is more likely to cause grinding. This is expected because more energy is being supplied by the faster attritor. However, as the proportionality of 7.5 mm media increases, the mean energy per collision decreases because smaller media have a lower individual mass. There is also an increase in collision frequency as **the proportion of 7.5 mm beads increases because total media volume was kept constant, meaning there a greater number of media and an increase in total surface area.**

If the trends are shown for different size ratios, Figure 13, the same patterns are observed but become more extreme as the size ratio increases. By the time the smaller media is reduced to 3.75 mm in Figure 13(d), a clear bimodal peak can be observed from the energies supplied by the different collision types. This can be validated in Figure 14, which splits each line into the individual collision types. There is a clear peak for contacts between two large, and two small media because of the mass differences, and the segregation which has been previously commented on, meaning that those mass fractions interact far more discretely than when the ratio is smaller. The contacts between a 10 mm and one of the smaller sizes span a wide range of energies compared to the ones for the single-size contacts. Within an industrial setting, this is very relevant because if media wear is causing size reduction and segregation of the media, shifting the energy curves to the left and reducing the probability of high energy, successful collisions and grinding potential.

Figures 12 and 13 have shown that there could be some compromise between having enough high-energy collisions from the large media and having a high frequency of collisions from the smaller media. Therefore the combined energy for each simulation was plotted in Figure 15, with different sections of each bar representing the individual collision types. The total collision frequency is also shown for reference (Figure 16). The increased number of contacts from the smaller media, particularly in the 3.75 mm case, (d), shows that there is a clear compromise point where the amount of grinding energy produced is higher. This is because there are more frequent collisions across the mill from the smaller size, but the quantity of large media is still high enough. There is also a significant contribution from impacts between a large and a small bead, suggesting the boundary is high enough to be within the pin region. Industrially this is highly significant because the media size could be controlled and topped up to get specific age and size distributions of the media and optimise energy transfer. Different sizes can also be added to the virgin media to aid this. **Wear profiles and correlations can be generated [62–65], with Altun *et al.* [20] being one such example in the mining industry. They correlated energy input to mass loss, meaning a rough size distribution can be found. The initial size going into the mill can also be controlled and does not have to be a single size, aiding a polydisperse size distribution.**

3.4.2. Energy distribution by height

The energy distributions were also plotted by height to show if there are any vertical differences because of the media segregation (Figure 17). The peak energy is just below the middle pair of pins for all simulations and then has a skewed Gaussian distribution. This makes sense because the middle pins are where the greatest energy input density is. For most cases, energy from contacts between 10 mm media dominates. It is only when high proportions of 7.5 mm and 5.0 mm media are used that the contribution of the smaller sizes dominates. In these cases, they are volumetrically dominant and responsible for the majority of contacts.

There is more energy below the pins than above as more media are at the bottom due to gravity. Even though it was identified as a lower velocity zone, the bottom 10 mm can contribute as much as $60\,\mathrm{J\,s^{-1}}$. As the size ratio increases, more contacts can fit within each cell and the bottom layer of media becomes smaller in average depth, reducing boundary effects. Within a mill, a layer of media cage at the outer surfaces, often having much slower kinetics than those slightly further inwards. If the media diameter is reduced, this layer becomes smaller. Therefore the perceived active region increases.

To draw a more direct comparison, the total energy by height has also been plotted linearly (Figure 18). At high size ratios, the profiles are very similar because the mill is mostly 10 mm media by volume, particularly within the pin region. At smaller size ratios, there are slight differences. Low proportions of 10 mm media produce a higher peak and greater total area. This agrees with the observations seen in Figure 17, where a 0.1 fraction of 10 mm media gives a slightly higher energy. At high proportions of 3.75 mm media, there is a significant rise in the peak stress energies observed. This is because there is still a large volume of 10 mm beads, but enough 3.75 mm beads to fill the spaces between them effectively. At large proportions of 10 mm media, the spaces between media and small gaps between attritor and vessel mean that the media are quite spaced and unable to transfer their momentum fully. Improved packing from a mix of sizes allows for more effective momentum transfer. These results give a good indication of optimal media distribution. A smaller base size with a handful of slightly larger media provides a strong result, suggesting that including multiple bead sizes increases the optimal grinding performance.

While overall stress energy contribution is important, milling relies on individual contacts having sufficient energy to reduce particle size successfully. Figure 19 and 20 show for each size ratio, the contact frequency and stress energy per contact. While Figure 18 shows a setup with balanced volumes of a higher size ratio as a potentially optimal choice, the energy per contact is much lower throughout the milling space. As explained, the smaller media carry much lower momentum, so transfer less energy through individual collisions. What is causing the large amounts of energy transfer is the much larger quantity of contacts recorded, particularly in the lower part of the mill where most of the volume is smaller media. For the most part, 10 mm media are present in large quantities and the number of contacts is similar at the top of the vessel because the segregation effects mean that the upper region is almost solely larger media. This changes very little until the smaller media are added in large quantities, especially when the size ratio increases.

This balance between high energy and high contact frequency is critical when designing a milling process, as it gives operators a very controllable way of optimising the overall energy distributions observed within the mill and can be tailored for specific materials and particle size specifications. The locations and size of the contacts also give further evidence that the flow of material in continuous processes should be from top to bottom so that finer particles can interact more with smaller media which produce a finer grind [9, 10]. This is not always the case, with many vertical mills preferring a pump-up approach as it maximised slurry residence time [66, 67].

3.5. Power draw

While most of the previous analysis has centred around the theoretical effectiveness of milling, the power draw can be used to determine the overall efficiency. The power has been calculated using the method described in Section 2.3.3, which assumes that the power draw equals the energy dissipated in each contact. The result for each simulation is shown in Figure 21. There are slight deviations in results because of the instantaneous nature of the sampling, but for each ratio, there are some common themes. In most cases, the power draw falls slightly as the smaller size is added until media quantities become roughly equiproportional. Then, as the smaller size becomes the dominant fraction the power increases and by the time the mill becomes exclusively smaller media, the power is slightly greater than when the mill is full of 10 mm media. There are more contacts when the mill contains smaller media, so there are more dissipative events. This is similar in most cases, apart from the 3.75 mm size fraction, Figure 21(d). There is a more significant power decrease at a much higher numerical proportionality. This is because at numerical ratios of 0.8-0.9, the 3.75 mm media mostly sit below the attritor pins, while in the attritor region, there are fewer of the 10 mm media to dissipate energy, than compared to a lower proportionality. However, the trend continues even when all of the media are of a smaller size. By this point, the media are small enough to behave more like a fluid body rather than as individual elements. This means the attritor has a lower profile when moving through the media, and the gaps between the attritor and vessel are large enough to fit several media. This is highly significant industrially, as reduced power draw and favourable collision kinetics suggest that a mixture of small and large media might be better than having a single media size.

As seen in previous studies [36, 40], there is a non-linear trend as the attritor velocity increases, which is to be expected as more energy is supplied. Radzizewski and Allen [53, 54] concluded that the power draw is proportional to the rotational velocity squared (Equation 10). The plots show a reasonable level of agreement with this, especially when considering that the power is also related to the shear volume, and this changes with velocity because different surfaces come into and out of contact with the media, hence why there is an inexact correlation to the squared velocity.

For each simulation, the stress energy was divided by the power draw (Figure 22). This shows that in most cases, the energies observed are proportional to the power supplied, meaning that an increase in attritor velocity linearly increases the energy generated. There is a lower efficiency at 50 rpm, meaning that the contacts are much lower in energy than the power used. Given that from Figure 21 the trends are non-linear, the stress energies are very low compared to higher attritor speeds. There is a special case where the efficiency is much higher. This is when the size ratio is high but there is a high quantity of smaller media. This is because the energy is maintained within the contacts and less is dissipated which is the calculation assumption. The smaller media are easier for the attritor to move through, reducing potential resistance and increasing single-body motion.

3.6. Full polydispersity

Three final simulations were run to see if the observed effects of the binary system also occurred when a fully polydisperse set of media was used. The first setup used an equal quantity of all six media sizes at 50 rpm, with an equivalent total volume to all prior simulations. The second was to use the same setup but at 250 rpm. The final one used equal volumes of each fraction, again filled to the same overall volume. All three were run for 60 seconds from the point of the first attritor movement, just like the steady state checks (Appendix B).

Figure 23 and Video 2 shows the progression of the simulation containing the same number of media at each size fraction. The media segregate as expected, with the larger fractions moving towards the free surface at the top. This is especially prevalent for the equal quantities simulation because most of the volume comprises the larger media. At the start, the small media percolate as they can move through the vortices formed from the other media packing together without the driving energy of the attritor. This is why they start at a lower centre of mass than other fractions, and fall towards their stable level very quickly. The larger media cannot do this and require other driving factors to move axially. This is why they take longer to reach a stable centre of mass and even after this has been reached, there is still a small amount of fluctuation.

As the velocity increases to 250 rpm, Figure 24 and Video 3, the same effect of segregation is seen. However, all of the media fractions sit higher than at 50 rpm, and this is due to the formation of the vortex in the centre of the mill. A convective remixing effect that is able to lift all media, but especially the smaller fractions sitting within the bottom section. The reason for the delayed response in the small fractions is that the mill was accelerated gradually, meaning the vortex took time to form initially. It forms from the free surface and then develops further down the vessel. This means the same initial percolation effect occurs, like in Figure 23, before convective remixing dominates and elevates the smaller media. The centrifugal force of the circular motion also means that media want to push outwards, and eventually upwards because they have nowhere else to move. This is especially true at the free surface because media are not obstructed by anything above, so elevate towards the upper section.

In contrast, Figure 25 and Video 4 show the result of putting all six media fractions in the mill with equivolume quantities. The full polydisperse nature of the simulation means that a densely packed bed is formed by the media, and at 50 rpm, the energy supplied is not enough to disturb the bottom layers that sit under the attritor. This is bad for grinding performance because energy is dissipated quickly, and is not transferring to all of the beads successfully, reducing the active milling region. Above the dead zone at the bottom, the media is largely segregated as seen previously but looks less separated on the centre of mass by time plot because of the effects of the lower region. There is still percolation from the small media but less of it because of the better media packing from the system.

A comparison of the contact energies for three cases is shown in Figure 26. The polydisperse case setup in Figure 24 falls somewhere in between the results of an equal count, low size ratio (7.5 mm media, 50%) and a high size ratio with significant count of small media (3.75 mm, 90% small) charge. Because of the segregation effects, the size ratios in the polydisperse case locally are quite low for the most part, but there will still be contacts between media of a high size ratio. Because there are three types of contact, the energy distribution, Figure 26(a), is much broader than in the other cases and does not show distinctive peaks like the high size ratio simulations do. The remaining distributions fall roughly in line with other setups, meaning the mill is performing consistently. It can also be seen that when plotting against height, the polydisperse case performs almost identically to the low size ratio case within the top 50 mm of the vessel. This is because the compositions are likely to be very similar in that it will mostly be 10 mm media with some 7.5 mm also present.

Industrially, vertical mills containing polydisperse media are the most likely to occur because of how they are operated and the natural ageing effects caused by bead wear. However, there is a possibility for this to be controlled more strictly to obtain a specific distribution that suits the application. Mineral processing for instance relies on high-impact contacts to break hard particles. Meanwhile, the food industry, where particles are softer, may utilise other size ratios and proportions with lower peak energies but a greater contribution due to the volume of contacts. As well as the observed effects, this research also highlights why simulations are becoming more relevant within research because they can very easily show that there can be inefficiencies within the mill and where it is within the equipment. This can lead to better designs of both the attritor and/or vessel to reduce or remove this effect.

4. Validity

From previous work [36, 40, 41], it was believed that the modelling parameters were most representative to characterise the motion of the media and inter-particle stresses. The aim was to show the effects of changing media size fractions in isolation, rather than try to replicate a specific industrial example which would cost thousands to validate experimentally. Therefore, the study was re-run with a restitution coefficient of 0.1 and friction coefficient of 0.9. Using low restitution and high friction was the opposite of the initial investigation, and qualitative agreement will show that the observations are independent of the other values used and can be considered valid, as all alternative combinations will fall in between the two cases demonstrated.

While there are some differences in the $3.75\,\mathrm{mm}$ **case, the Lacey index in most cases remains largely unchanged compared to the original (Figure 7), particularly at higher speeds (Figure 27). The high friction increases the Lacey index at lower speeds due to the resistance of some of the percolation drivers. When the size ratio is smaller, Figure 27(a), the effects are similar to the original plot because the reduced segregation in these simulations is less affected**

by the change of resistance.

One of the major findings was that there is a compromise between lots of contacts between smaller media and some high-impact collisions from the larger beads. If this plot is presented again with the new parameters, as shown in Figure 28, the results qualitatively suggest the same trend as in Figure 15. However, there is a slight shift in where the peak energy is as a proportion due to the changes in the Lacey index previously discussed. In the 3.75 mm simulations, the peak shifts from a large media fraction of 0.1 to 0.3 but the same information can otherwise be extracted in the same way as the original parameters. There is a compromise between having many high-impact contacts and having a high quantity of contacts which qualitatively agrees with the initial batches.

The results of Figure 27 and 28 show that the main qualitative findings are independent of specific media properties and therefore can be deemed valid for this trial. The only thing which is changing is the magnitude of the values and optimal population, although neither varies significantly from the original conditions,

5. Conclusion

The paper has detailed the effects of changing the proportion and size ratio of a binary dispersed set of grinding media within a vertical stirred mill. Overall, three main conclusions can be drawn:

1. Including a mix of large and small grinding media increases the total stress energy observed, as both high-impact collisions

from the large media and a high contact frequency from lots of small media are present.

2. Having a high proportion of small media reduces the power draw by reducing the contact distance between media. This might improve the overall energy efficiency but we need to understand the grinding effect. This is proposed for future study.

3. Segregation of different media sizes is advantageous, as it creates different collision types within the mill. Larger media produce higher energy contacts to break larger particles while smaller media can produce a finer grind, so if the slurry flow can be directed from the top of the mill to the bottom, it maximises the effectiveness throughout the system.

The scope of the study has been limited to changing the media size so that the effects observed could be isolated to a single variable. To demonstrate the validity of the results, the investigation was repeated using highly contrasting media properties and qualitatively, they agree with the initial study (See Section 4). While we understand that operators control the mill using different measures to the ones analysed, what we are doing with the simulation approach is predicting the parameters which would provide strong grinding potential. This reduces the number of physical trials which would then be required to reach an optimal set of operating conditions because there is a greater understanding of the

contact dynamics before online operation. Further investigations looking at shape and surface property variation between media, and wear of both media and attritor as a function of time would have increased the reality of the model. However, these would also have increased the complexity of modelling and analysing the effects of changing multiple parameters simultaneously.

Declaration of Competing Interest

The authors declare upon submission that there are no competing interests.

Acknowledgements

The corresponding author is studying for an Engineering Doctorate (EngD) at the University of Birmingham and acknowledges funding from the Centre for Doctoral Training in Formulation Engineering via the Engineering and Physical Sciences Research Council and Mondelēz International. (EPSRC Grant no. EP/S023070/1). The simulations were performed using the University of Birmingham's BlueBEAR HPC service, which provides a High-Performance Computing service to the University's research community. See `http://www.birmingham.ac.uk/bear` for more details.

654 ## Nomenclature

A	Shear area	m^2
E	Young's Modulus	Pa
E^*	Effective Young's Modulus	Pa
F_{ij}^n	Normal contact force	N
F_{ij}^t	Tangential contact force	N
G	Shear Modulus	Pa
G^*	Effective Shear Modulus	Pa
g	Gravitational acceleration	$\mathrm{m\,s^{-2}}$
I	Moment of inertia	$\mathrm{kg\,m^2}$
K^n	Normal stiffness	$\mathrm{N\,m^{-1}}$
K^t	Tangential stiffness	$\mathrm{N\,m^{-1}}$
m	Particle mass	kg
m^*	Effective particle mass	kg
P_n	nth Percentile	-
R	Particle radius	m
R^*	Effective particle radius	m
r_s	Shear radius	m
S^n	DEM contact law constant	-
t	Timestep	s
V_τ	Shear volume	m^3
v_{ij}^n	Relative normal velocity	$\mathrm{m\,s^{-1}}$
v_{ij}^t	Relative tangential velocity	$\mathrm{m\,s^{-1}}$
β	DEM contact law constant	-
γ^n	Normal damping coefficient	$\mathrm{N\,s\,m^{-1}}$
γ^t	Tangential damping coefficient	$\mathrm{N\,s\,m^{-1}}$
δ_{ij}^n	Normal particle overlap	m
δ_{ij}^t	Tangential particle overlap	m
ε	Coefficient of restitution	-
η	Dynamic viscosity	Pa s
ν	Poisson ratio	-
ρ	Particle density	$\mathrm{kg\,m^{-3}}$
τ_{ij}^t	Rolling friction coefficient	-
ω	Rotational velocity	$\mathrm{rad\,s^{-1}}$

Appendix A: Additional Equations

From Section 2.1, the normal and tangential forces between a pair of colliding particles, F_{ij}^n and F_{ij}^t respectively, were defined. [38, 40]

$$F_{ij}^n = K^n \cdot \delta_{ij}^n - \gamma^n \cdot v_{ij}^n, \tag{3}$$

$$F_{ij}^t = K^t \cdot \delta_{ij}^t - \gamma^t \cdot v_{ij}^t. \tag{4}$$

For each equation, the total force is made up of the difference between the elastic and dissipative components in that direction. Starting with the normal force (Equation 3), the elastic component is found by multiplying the normal overlap between the particles, δ_{ij}^n by the stiffness constant, K^n, which is found in Equation 12,

$$K^n = \frac{4}{3} E^* \sqrt{R^* \delta_{ij}^n}. \tag{12}$$

E^* is the effective Young's modulus between particles, with E_i and E_j being the individual moudii.

$$E^* = \left(\frac{1 - \nu_i^2}{E_i} + \frac{1 - \nu_j^2}{E_j} \right)^{-1}, \tag{13}$$

and R^* is the effective radius,

$$R^* = \frac{R_i R_j}{R_i + R_j}. \tag{14}$$

ν is the Poisson ratio of each particle. The dissipative component of Equation 3 is calculated from the relative normal velocity of the particles v_{ij}^n, which is multiplied by the dissipative coefficient, γ^n.

$$\gamma^n = -2\sqrt{\frac{5}{6}}\beta\sqrt{S^n m^*} \cdot v_{ij}^n. \tag{15}$$

S^n is described in Equation 16 [68],

$$S^n = 2E^*\sqrt{R^*\delta_{ij}^n}, \tag{16}$$

β is a proportionality constant, with ϵ being the particle restitution coefficient,

$$\beta = \frac{\ln(\varepsilon)}{\sqrt{\varepsilon^2 + \pi^2}}. \tag{17}$$

and lastly, m^* is the effective particle mass,

$$m^* = \frac{m_i m_j}{m_i + m_j}. \tag{18}$$

The tangential force equation (Equation 4), follows the same basic philosophy as for the normal force. This time, δ_{ij}^t represents the tangential overlap and this is multiplied by the tangential elastic coefficient to get the elastic component of the collision force,

$$K^t = 8G^*\sqrt{R^*\delta_{ij}^n}. \tag{19}$$

G^* is the effective shear modulus and is calculated in a similar way to the effective Young's modulus,

$$G^* = \left(\frac{1-\nu_i^2}{G_i} + \frac{1-\nu_j^2}{G_j}\right)^{-1}. \tag{20}$$

To calculate the dissipative component, the relative tangential velocity, v_{ij}^t, is multiplied by the tangential stiffness constant, K^t,

$$\gamma^t = -2\sqrt{\frac{5}{6}}\beta\sqrt{K^t m^*} \cdot v_{ij}^t. \tag{21}$$

Equations 3 and 4 form the basis for calculating power draw because the normal and tangential forces for each contact are provided in the LIGGGHTS output data. It is assumed that the power draw is equivalent to the energy dissipated in the system.

Appendix B: Steady state checking

Because the grinding media were inserted into the mill randomly and then allowed to move and segregate freely, a check had to be done to ensure a comparable state had been reached for all simulations. This was done by running three additional simulations using the worst mixing conditions. These are stated:

- 10 mm vs 7.5 mm particles (smallest media ratio)
- equal proportionality (zero proportionality bias)
- 50 rpm rotational speed (slowest attritor rotation)

The progression of these simulations is shown in Figure 29 and Video 1. The grinding media were seeded in different ways: all of the 10 mm media first, (a), randomly, (b), and all of the 7.5 mm beads first, (c). The reason was that barring equipment inefficiency, all three should naturally converge to a similar state due to entropy, and the time taken would be useful in determining whether the ten-second period stated was long enough for the majority of simulations to normalise. Overall, the three simulations tend towards a similar state and except for a handful of media, almost completely segregate. Figure 30 shows the progression numerically by taking the vertical centre of mass for each media fraction. For each case, the fractions segregated, and eventually stabilised to within a constant level. However, they do not all align perfectly because of the dead zone at the bottom of the mill, as stated in Section 5. This section largely resembles its initial fill state and fractionally adjusts the overall averages seen. Even at 60 seconds, Figure

29 shows that the bottom layer of media has been largely unaffected while everything above has almost completely segregated. It is also unsurprising that in the instance where small media were filled first, this is the first case to reach a steady state as the media are already naturally segregated.

What Figure 29, 30 and Video 1 prove is that the ten seconds analysed is appropriate, as despite the mills having not reached full stability in the cases presented, the changes by the end are fairly insignificant from the final result. This is also the worst-case assumption, so other simulations are expected to segregate faster. The centre of mass for the mixed fill is less than 2 mm difference from the full stability of the simulation so further changes are minimal. Therefore, the period suggested for analysis (shaded in Figure 30) has been deemed appropriate for all simulations.

To further prove that the simulations have reached a steady state, the segregation progression of the 7.5 mm simulations at 50 rpm is shown (Figure 30). These show that the average z-position starts from the same point and then spreads as the two fractions segregate. Higher proportions of 7.5 mm media push the average height of both fractions up because of the greater volume of smaller beads. Most importantly, the simulations reach an approximate steady state by the analysis period, allowing for some natural fluctuation. This further proves that the period for further analysis is appropriate and that the starting point should be after 45 seconds.

Appendix C: Sub-region analysis

Another way to check for segregation is to consider media within specific sub-regions of the mill. Three cases were run, shown in Figure 31, with red sections denoting areas not considered in a particular set of analyses. The sub-region only considering the pins, Figure 31(b), was because this is theoretically where the highest energy media should be because the pins supply the energy to the mill. Meanwhile, Figure 31(c) did not consider a region previously identified as containing media with significantly lower kinetics than the rest of the design [40].

As Figure 30 showed, there is significantly less movement at the bottom of the vessel because it is below the bottom of the attritor. If this region is removed, as represented in Figure 31(c), the fraction of media which remains changes significantly in some cases (Figure 32). In almost all cases, a minimum of 20% of the media total sits within this dead zone. However, the worst case is when 40% of 3.75 mm media are included, where this value drops to just 40% of media sitting above the bottom 20 mm of the vessel height. This is bad design that such a large proportion of media sit within a sub-optimal grinding region.

Figure 33 plots the same proportionality but for the media in the pin region. These charts show what fraction of the media are in the most effective region of the mill for energy transfer. The proportion of media in line with the pins varies based on velocity and size ratio. As you add smaller media, they segregate toward the bottom of the mill, and with more being able to fit into the same volume as the larger size, reduce the number within the pin region. **The greater attrition coming from smaller media [4] will**

also cause more wear on the lower attritor pins, as demonstrated by Altun *et al.* [20] who observed 2.5 times the amount of wear on the bottom pins of a HIGMill compared to the top ones. This becomes more extreme when higher size ratios are considered because the smaller size takes up a lower overall volume despite being kept in constant numerical proportions. Increasing the rotational velocity also reduces the proportion between the pins. However, this is due to the increased centrifugal force pushing media into the region above the pins.

Within Figure 33(d), there is a linear trend at low rotational velocity and high 10 mm media proportionality. This is because almost all of the 3.75 mm media percolate to the bottom, as seen in Figure 32(d), and take up such a small amount of the total fill volume that the fraction observed is very close to the proportion of 10 mm media less a constant volume above and below the pins.

References

[1] J. de Bakker, Energy use of fine grinding in mineral processing, Metallurgical and Materials Transactions 1 (2014) 8–19. doi:10.1007/s40553-013-0001-6.

[2] C. Alamprese, L. Datei, Q. Semeraro, Optimization of processing parameters of a ball mill refiner for chocolate, Journal of Food Engineering 83(4) (2007) 629–636. doi:10.1016/j.jfoodeng.2007.04.014.

[3] A. Jankovic, T. Wills, S. Dikmen, A comparison of wear rates of ball

mill grinding media, Journal of Mining and Metallurgy A: Mining 52 (1) (2016) 1–10. doi:10.5937/JMMA1601001J.

[4] N. Matsanga, W. Nheta, N. Chimwani, Grinding media in ball mills - a review, Preprints (2023040811) (2023). doi:10.20944/preprints202304.0811.v1.

[5] B. Shahbazi, M. Jafari, M. Parian, J. Rosenkranz, S. Chehreh Chelgani, Study on the impacts of media shapes on the performance of tumbling mills – a review, Minerals Engineering 157 (2020) 106490. doi:10.1016/j.mineng.2020.106490.

[6] O. Altun, O. Darılmaz, E. Karahan, T. Sert, D. Altun, A. Toprak, A. Hür, Understanding higmill operation at copper regrind application; operating parameters, wear and mineral liberation, Minerals Engineering 191 (2023) 107964. doi:10.1016/j.mineng.2022.107964.

[7] F. Shi, Comparison of grinding media—cylpebs versus balls, Minerals Engineering 17 (11) (2004) 1259–1268, communition '04. doi:10.1016/j.mineng.2004.05.019.

[8] H. Cho, J. Kwon, K. Kim, M. Mun, Optimum choice of the make-up ball sizes for maximum throughput in tumbling ball mills, Powder Technology 246 (2013) 625–634. doi:https://doi.org/10.1016/j.powtec.2013.06.026.

[9] T. Napier-Munn, S. Morrell, R. Morrison, T. Kojovic, Mineral comminution circuits: their operation and optimisation, 1996.

[10] G. C. Edwards, Investigation of operating parameters in a vertical stirred mill, Ph.D. thesis, University of Cape Town (2016).

[11] A. Jankovic, Variables affecting the fine grinding of minerals using stirred mills, Minerals Engineering 16 (4) (2003) 337–345. doi:10.1016/S0892-6875(03)00007-4.

[12] K. Kabezya, H. Motjotji, The effect of ball size diameter on milling performance, Journal of Material Sciences & Engineering 2015 (2015) 1–3.

[13] M. Mankosa, G. Adel, R. Yoon, Effect of media size in stirred ball mill grinding of coal, Powder Technology 49 (1) (1986) 75–82. doi:10.1016/0032-5910(86)85008-2.

[14] L. Blecher, A. Kwade, J. Schwedes, Motion and stress intensity of grinding beads in a stirred media mill. part 1: Energy density distribution and motion of single grinding beads, Powder Technology 86 (1) (1996) 59–68. doi:10.1016/0032-5910(95)03038-7.

[15] A. Kwade, L. Blecher, J. Schwedes, Motion and stress intensity of grinding beads in a stirred media mill. part 2: Stress intensity and its effect on comminution, Powder Technology 86 (1) (1996) 69–76. doi:https://doi.org/10.1016/0032-5910(95)03039-5.

[16] H. Fadhel, C. Frances, Wet batch grinding of alumina hydrate in a stirred bead mill, Powder Technology 119 (2-3) (2001) 257–268.

[17] A. Kumar, R. Sahu, S. K. Tripathy, Energy-efficient advanced ultra-fine grinding of particles using stirred mills—a review, Energies 16 (14) (2023). doi:10.3390/en16145277.

[18] M. D. Sinnott, P. W. Cleary, R. D. Morrison, Is media shape important for grinding performance in stirred mills?, Minerals Engineering 24 (2) (2011) 138–151. doi:10.1016/j.mineng.2010.10.016.

[19] C. Jayasundara, R. Yang, A. Yu, Effect of the size of media on grinding performance in stirred mills, Minerals Engineering 33 (2012) 66–71, computational Modelling. doi:https://doi.org/10.1016/j.mineng.2011.10.012.

[20] O. Altun, H. Benzer, U. Enderle, Effects of operating parameters on the efficiency of dry stirred milling, Minerals Engineering 43-44 (2013) 58–66, sI: Comminution. doi:10.1016/j.mineng.2012.08.003.

[21] B. Farber, B. Durant, N. Bedesi, Effect of media size and mechanical properties on milling efficiency and media consumption, Minerals Engineering 24 (3) (2011) 367–372, special issue: Comminution. doi:10.1016/j.mineng.2010.10.018.

[22] S. Mende, F. Stenger, W. Peukert, J. Schwedes, Production of submicron particles by wet comminution in stirred media mills, Journal of Material Science 39 (16) (2004) 5223–5226. doi:10.1023/B:JMSC.0000039214.12131.58.

[23] C. Eswaraiah, N. Venkat, B. Mishra, R. Holmes, A comparative study on a vertical stirred mill agitator design for fine grinding, Separation

Science and Technology 50 (17) (2015) 2639–2648. doi:10.1080/01496395.2015.1065888.

[24] L. Orozco, D.-H. Nguyen, J.-Y. Delenne, P. Sornay, F. Radjai, Discrete-element simulations of comminution in rotating drums: Effects of grinding media, Powder Technology 362 (2020) 157–167. doi:https://doi.org/10.1016/j.powtec.2019.12.014.

[25] R. Soni, B. Mishra, Understanding size segregation in tumbling mills, in: X. Li, Y. Feng, G. Mustoe (Eds.), Proceedings of the 7th International Conference on Discrete Element Methods, Springer Singapore, Singapore, 2017, pp. 1153–1168.

[26] B. Yari, C. Beaulieu, P. Sauriol, F. Bertrand, J. Chaouki, Size segregation of bidisperse granular mixtures in rotating drum, Powder Technology 374 (2020) 172–184. doi:10.1016/j.powtec.2020.07.030.

[27] P. Tang, V. Puri, Segregation quantification of two-component particulate mixtures: Effect of particle size, density, shape, and surface texture, Particulate Science and Technology 25 (6) (2007) 571–588. doi:10.1080/02726350701783977.

[28] A. Tripathi, D. Khakhar, Density difference-driven segregation in a dense granular flow, Journal of Fluid Mechanics 717 (2013) 643–669. doi:10.1017/jfm.2012.603.

[29] C. Windows-Yule, T. Weinhart, D. Parker, A. Thornton, Effects of packing density on the segregative behaviors of granular systems, Physical review letters 112 (9) (2014) 098001.

[30] C. Windows-Yule, D. Parker, Inelasticity-induced segregation: Why it matters, when it matters, EPL (Europhysics Letters) 106 (6) (2014) 64003.

[31] C. Windows-Yule, D. Parker, Density-driven segregation in binary and ternary granular systems, KONA Powder and Particle Journal 32 (2015) 163–175. doi:10.14356/kona.2015004.

[32] C. Windows-Yule, Convection and segregation in fluidised granular systems exposed to two-dimensional vibration, New Journal of Physics 18 (3) (2016) 033005. doi:10.1088/1367-2630/18/3/033005. URL https://doi.org/10.1088/1367-2630/18/3/033005

[33] C. Windows-Yule, B. Scheper, A. van der Horn, N. Hainsworth, J. Saunders, D. Parker, A. Thornton, Understanding and exploiting competing segregation mechanisms in horizontally rotated granular media, New Journal of Physics 18 (2) (2016) 023013. doi:10.1088/1367-2630/18/2/023013.

[34] P. Cundall, O. Strack, A discrete numerical model for granular assemblies, Geotechnique 29(1) (1979) 47–65.

[35] Y. Zhou, B. Wright, R. Yang, B. Xu, A. Yu, Rolling friction in the dynamic simulation of sandpile formulation, Physica A 269 (1999) 536–543. doi:10.1016/S0378-4371(99)00183-1.

[36] D. Daraio, J. Villoria, A. Ingram, A. Alexiadis, E. Stitt, M. Marigo, Investigating grinding media dynamics inside a vertical stirred mill using

the discrete element method: Effect of impeller arm length, Powder Tech 364 (2020) 1049–1061. doi:10.1016/j.powtec.2019.09.038.

[37] EDEM, EDEM 2.6 theory reference guide, https://www.edemsimulation.com/content/uploads/2016/08/EDEM2.6_theory_reference_guide.pdf, [Accessed: 2021-02-28] (2014).

[38] N. Weerasekara, L. Liu, M. Powell, Estimating energy in grinding using DEM modelling, Minerals Engineering 85 (2016) 23–33. doi:10.1016/j.mineng.2015.10.013.

[39] CFDEM, LIGGGHTS open source discrete element method particle simulation code, https://www.cfdem.com/liggghts-open-source-discrete-element-method-particle-simulation-code, [Accessed: 2021-01-06] (2021).

[40] D. Rhymer, A. Ingram, K. Sadler, C. Windows-Yule, A discrete element method investigation within vertical stirred milling: Changing the grinding media restitution and sliding friction coefficients, Powder Technology 410 (2022) 117825. doi:10.1016/j.powtec.2022.117825.

[41] R. W. Rydin, D. Maurice, T. H. Courtney, Milling dynamics: Part i. attritor dynamics: Results of a cinematographic study, Metallurgical Transactions A 24 (1993) 175–185.

[42] M. Lucisano, E. Casiraghi, M. Mariotti, Influence of formulation and processing variables on ball mill refining of milk chocolate, European Food Research and Technology 223 (2006) 797–802. doi:10.1007/s00217-006-0272-6.

[43] A. de Oliveira, R. de Carvalho, L. Tavares, Predicting the effect of operating and design variables in grinding in a vertical stirred mill using a mechanistic mill model, Powder Technology 387 (2021) 560–574. doi:10.1016/j.powtec.2021.04.057.

[44] M. Sinnott, P. W. Cleary, R. Morrison, Analysis of stirred mill performance using dem simulation: Part 1 – media motion, energy consumption and collisional environment, Minerals Engineering 19 (2006) 1537–1550. doi:10.1016/j.mineng.2006.08.012.

[45] P. W. Cleary, Predicting charge motion, power draw, segregation and wear in ball mills using discrete element methods, Minerals Engineering 11 (1998) 1061–1080. doi:10.1016/S0892-6875(98)00093-4.

[46] C. Thornton, C. Randall, Applications of theoretical contact mechanics to solid particle simulation, Elsevier, 1988, pp. 133–142. doi:10.1016/B978-0-444-70523-5.50023-0.

[47] BlueBEAR, Bluebear standard resources, https://docs.bear.bham.ac.uk/bluebear/resources/#total-available-resources, [Accessed: 2024-02-02] (2024).

[48] X. Wu, Z. Zuo, S. Gong, X. Lu, G. Xie, Numerical study of size-driven segregation of binary particles in a rotary drum with lower filling level, Advanced Powder Technology 32 (12) (2021) 4765–4778. doi:10.1016/j.apt.2021.10.028.

[49] N. Govender, R. Rajamani, D. Wilke, C.-Y. Wu, J. Khinast, B. Glasser, Effect of particle shape in grinding mills using a gpu based dem code,

Minerals Engineering 129 (2018) 71–84. doi:10.1016/j.mineng.2018.09.019.

[50] P. Lacey, Developments in the theory of particle mixing, Journal of Applied Chemistry 4 (5) (1954) 257–268. doi:https://doi.org/10.1002/jctb.5010040504.

[51] S.-H. Chou, Y.-L. Song, S.-S. Hsiau, A study of the mixing index in solid particles, KONA Powder and Particle Journal 34 (2017) 275–281. doi:10.14356/kona.2017018.

[52] S. Beinert, G. Fragnière, C. Schilde, A. Kwade, Analysis and modelling of bead contacts in wet-operating stirred media and planetary ball mills with cfd-dem simulations, Chemical Engineering Science 134(2015) (2015) 648–662. doi:10.1016/j.ces.2015.05.063.

[53] P. Radziszewski, Assessing the stirred mill design space, Minerals Engineering 41 (2013) 9–16. doi:10.1016/j.mineng.2012.10.012.

[54] P. Radziszewski, J. Allen, Towards a better understanding of stirred milling technologies - estimating power consumption and energy use, in: The 46th Annual Canadian Mineral Processors Operators Conference, 2014, pp. 55–66.

[55] M.-W. Gao, K. S. E. Forssberg, K. R. Weller, Power predictions for a pilot scale stirred mill, International journal of Mineral Processing 44-45 (1996) 641–652. doi:10.1016/0301-7516(95)00072-0.

[56] T. Osborne, D. Rhymer, D. Werner, A. Ingram, C. Windows-Yule, Investigating the impact of impeller geometry for a stirred mill using the

discrete element method: Effect of pin number and thickness, Powder Technology 428 (2023) 118810. doi:https://doi.org/10.1016/j.powtec.2023.118810.

[57] Paraview, Welcome to paraview, https://www.paraview.org/, [Accessed: 2020-11-20] (2020).

[58] Blender, Home, https://www.blender.org/, [Accessed: 2021-03-02] (2021).

[59] A. Rosato, C. Windows-Yule, Chapter 5 - segregation measures, in: A. Rosato, C. Windows-Yule (Eds.), Segregation in Vibrated Granular Systems, Academic Press, 2020, pp. 93–102. doi:https://doi.org/10.1016/B978-0-12-814199-1.00011-1.

[60] A. Jankovic, Media stress intensity analysis for vertical stirred mills, Minerals Engineering 14 (10) (2001) 1177–1186. doi:10.1016/S0892-6875(01)00135-2.

[61] B. Francis, Scale-up and operations of a vertical stirred mill, Ph.D. thesis, University of British Columbia (2014). doi:10.14288/1.0165882.

[62] P. Radziszewski, Exploring total media wear, Minerals Engineering 15 (12) (2002) 1073–1087. doi:10.1016/S0892-6875(02)00228-5.

[63] H. Benavente, Correlacion empirica para estimar consumos de medios demolienda, X Simposium de Molienda Moly-Cop (2007).

[64] A. Sabih, P. Radziszewski, I. Mullany, Investigating grinding media differences in microstructure, hardness, abrasion and fracture toughness, Minerals Engineering 103-104 (2017) 43–53, sI: Comminution '16. doi:10.1016/j.mineng.2016.08.014.

[65] L. Guzmán, C. Rabanal, Updated benavente correlation for estimating grinding media consumption rates, IMPC 2014 - 27th International Mineral Processing Congress (01 2014).

[66] D. B. Mazzinghy, C. L. Schneider, V. K. Alves, R. Galéry, Vertical mill simulation applied to iron ores, Journal of Materials Research and Technology 4 (2) (2015) 186–190. doi:10.1016/j.jmrt.2014.10.011.

[67] R. M. de Carvalho, A. L. R. Oliveira, H. A. Petit, L. M. Tavares, Comparing modeling approaches in simulating a continuous pilot-scale wet vertical stirred mill using pbm-dem-cfd, Advanced Powder Technology 34 (9) (2023) 104135. doi:10.1016/j.apt.2023.104135.

[68] S. Yeom, E.-S. Ha, M.-S. Kim, S. H. Jeong, S.-J. Hwang, D. H. Choi, Application of the discrete element method for manufacturing process simulation in the pharmaceutical industry, Pharmaceutics 11 (8) (2019).

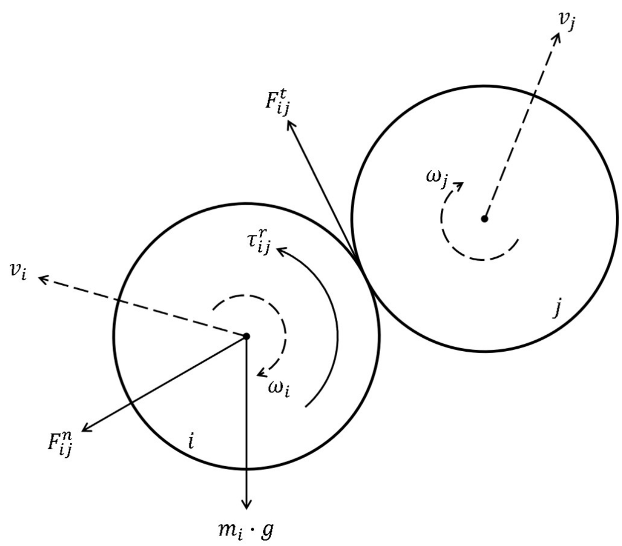

Figure 1: The resultant forces and torques of two particles, i and j, each of radius, r, in contact with each other [40]

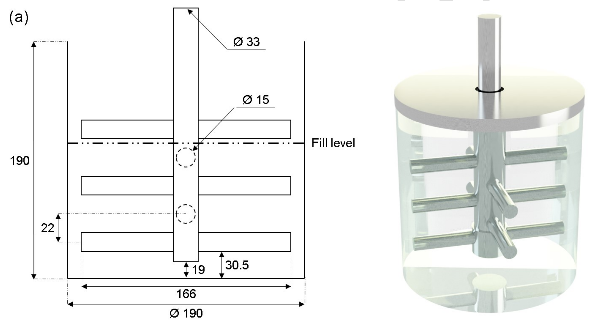

Figure 2: (a) Schematic representation of the mill with all key dimensions marked in millimetres. (b) 3D CAD model of the mill used [40].

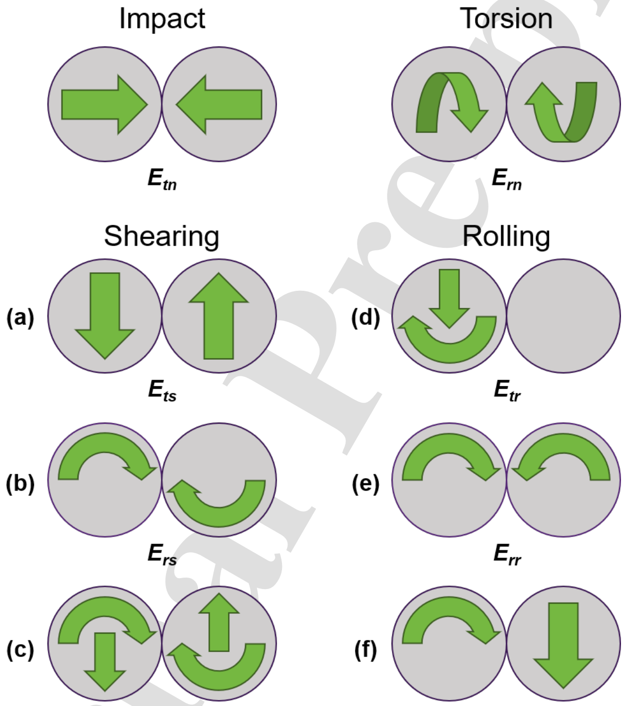

Figure 3: The eight collision mechanisms presented by Beinert *et al.* [52], separated into impact, torsion, shearing ((a)-(c)) and rolling ((d)-(f)) effects [40].

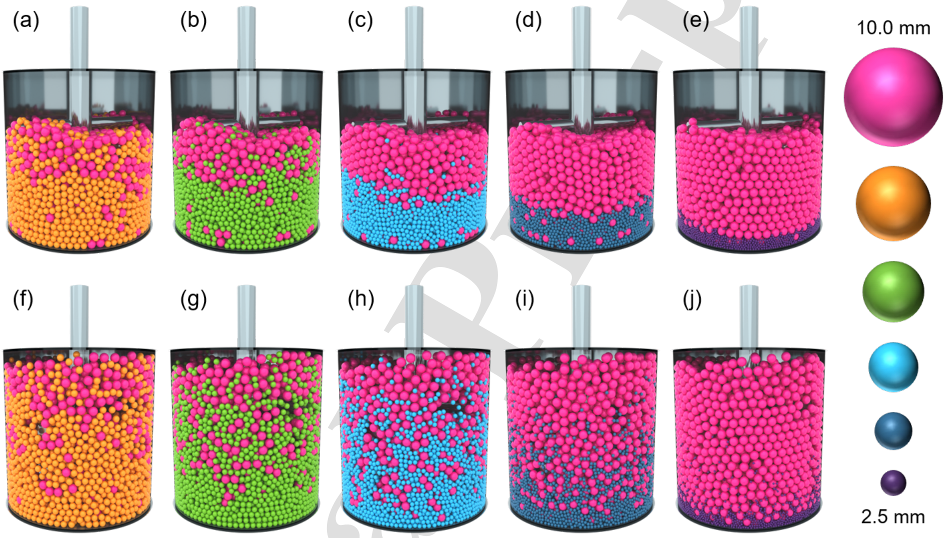

Figure 4: Images showing the state of 80% by quantity of different size media beads after 10 s of milling. (a) & (i) 7.5 mm, (b) & (g) 6.25 mm, (c) & (h) 5.0 mm, (d) & (i) 3.75 mm and (e) & (j) 2.5 mm. (a)-(e) are at 50 rpm, while (f)-(j) are at 250 rpm.

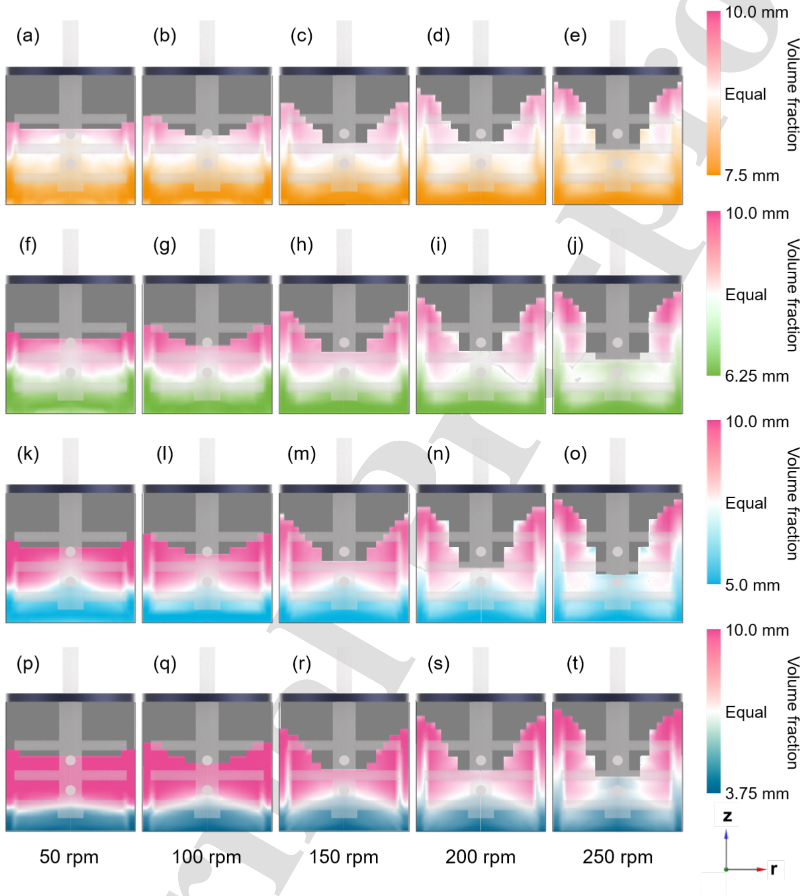

Figure 5: Time averaged volume occupancy fraction plots for an 80% count of the smaller media fraction. (a)-(e) 7.5 mm, (f)-(j) 6.25 mm, (k)-(o) 5.0 mm and (p)-(t) 3.75 mm. The rotational velocity increases from 50 rpm on the left to 250 rpm on the right of each row. Dark grey areas are empty.

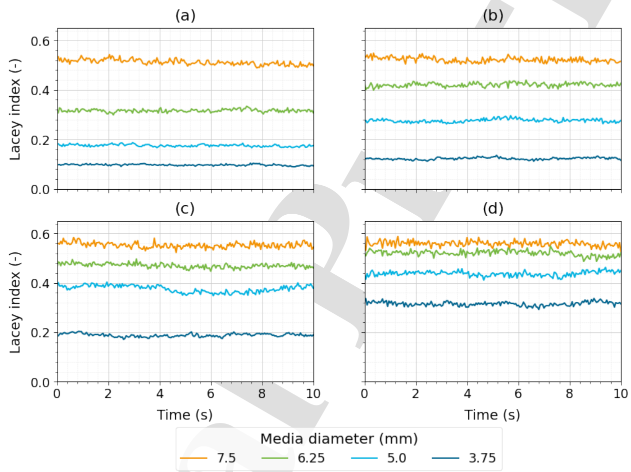

Figure 6: Progression of Lacey mixing index values over time for different simulations. (a) 50 rpm, (b) 100 rpm, (c) 150 rpm, (d) 200 rpm.

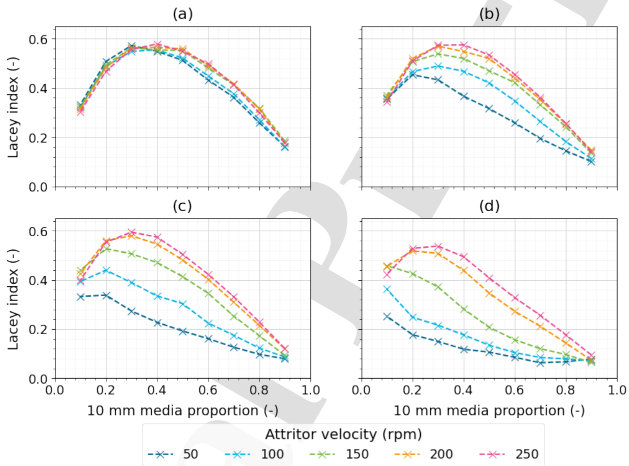

Figure 7: Calculated Lacey mixing indices for each simulation, plotted against count proportion. (a) 7.5 mm, (b) 6.25 mm, (c) 5.0 mm, and (d) 3.75 mm.

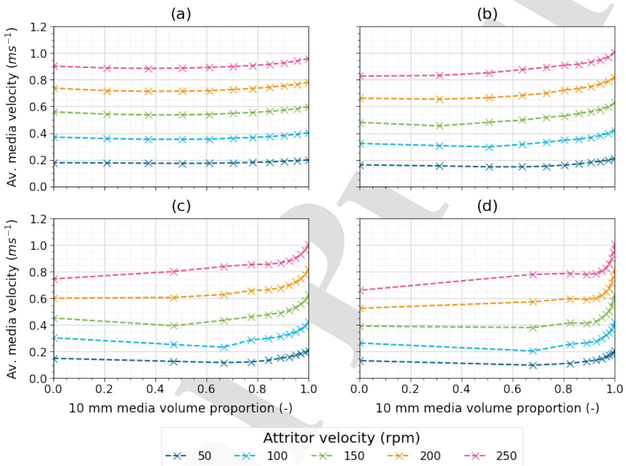

Figure 8: Plots showing the average media velocity at different attritor velocities for different volumetric media proportions. Smaller size media: (a) 7.5 mm, (b) 6.25 mm (c) 5.0 mm, (d) 3.75 mm.

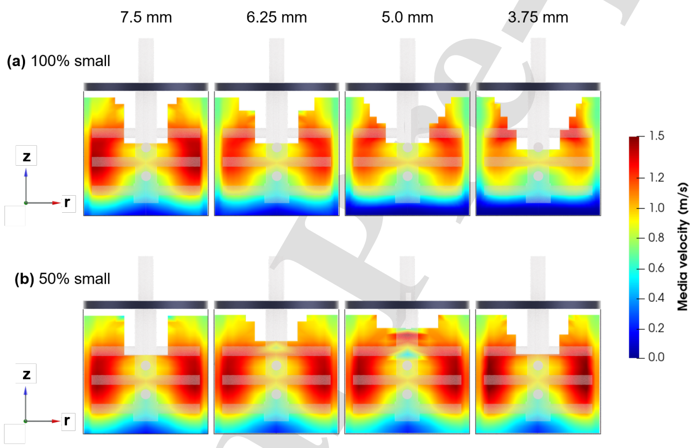

Figure 9: θ-averaged velocity field maps of the mill for different media proportions and size ratios at 250 rpm. (a) 100% small media, (b) 50% small media.

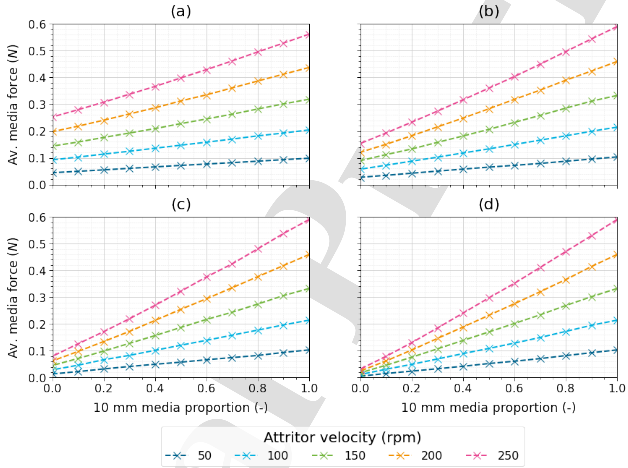

Figure 10: Linear force plots by media count proportion and velocity. (a) 7.5 mm, (b) 6.25 mm, (c) 5.0 mm, (d) 3.75 mm.

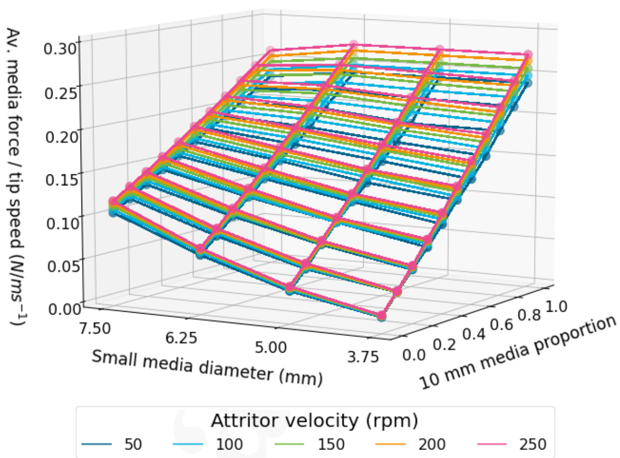

Figure 11: 3D planes showing the average media force, normalised by attritor tip speed for different media sizes and proportions.

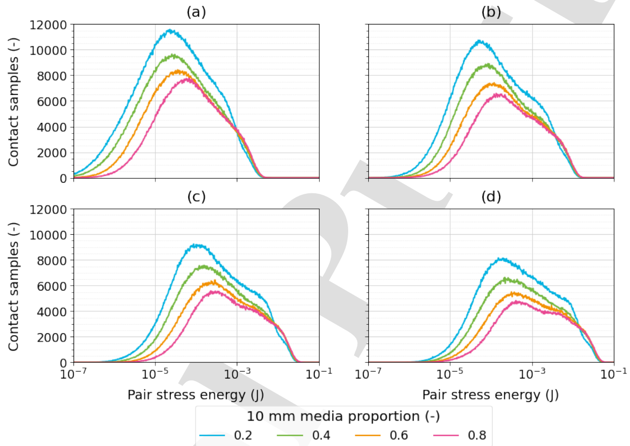

Figure 12: Overall collision energy spectra for different proportions of 10 mm vs 7.5 mm beads at different rotational velocities. (a) 50 rpm, (b) 100 rpm, (c) 150 rpm, (d) 200 rpm.

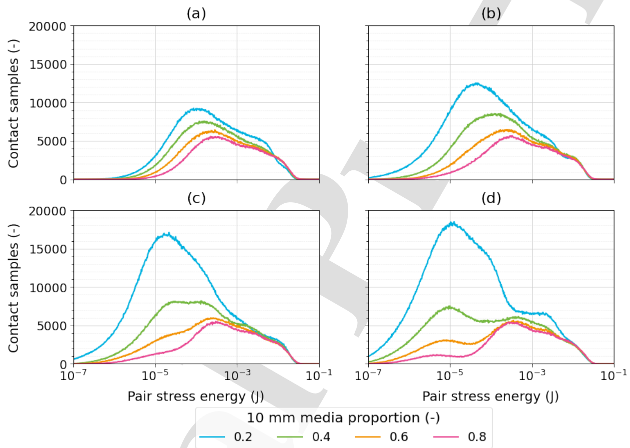

Figure 13: Overall collision energy spectra for different fractions of media beads at 150 rpm with different small sizes used. (a) 7.50 mm, (b) 6.25 mm, (c) 5.00 mm, (d) 3.75 mm

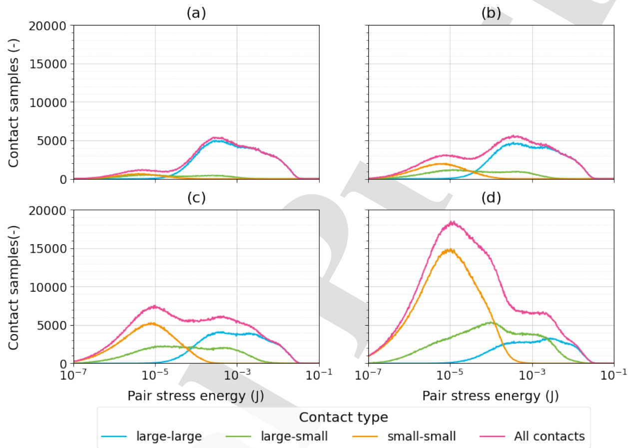

Figure 14: Collision energy spectra by collision type at different size proportionalities at 150 rpm (Breakdown of Figure 13(d)). (a) 20% small media, (b) 40% small media, (c) 60% small media, (d) 80% small media. All plots are for mills run at 200 rpm.

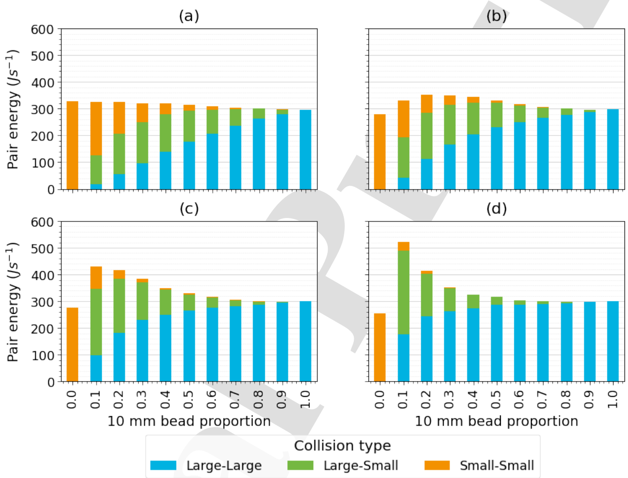

Figure 15: Overall collision energy spectra for different bead proportions and ratios at 250 rpm. (a) 7.5 mm, (b) 6.25 mm, (c) 5.0 mm and (d) 3.75 mm.

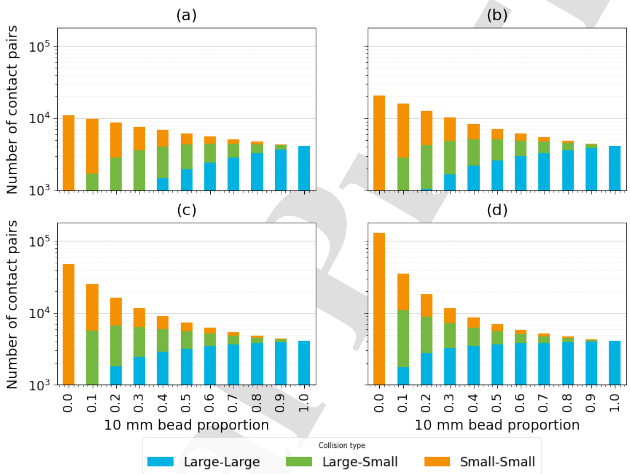

Figure 16: Average number of contact pairs for different bead proportions and ratios at 250 rpm. (a) 7.5 mm, (b) 6.25 mm, (c) 5.0 mm and (d) 3.75 mm.

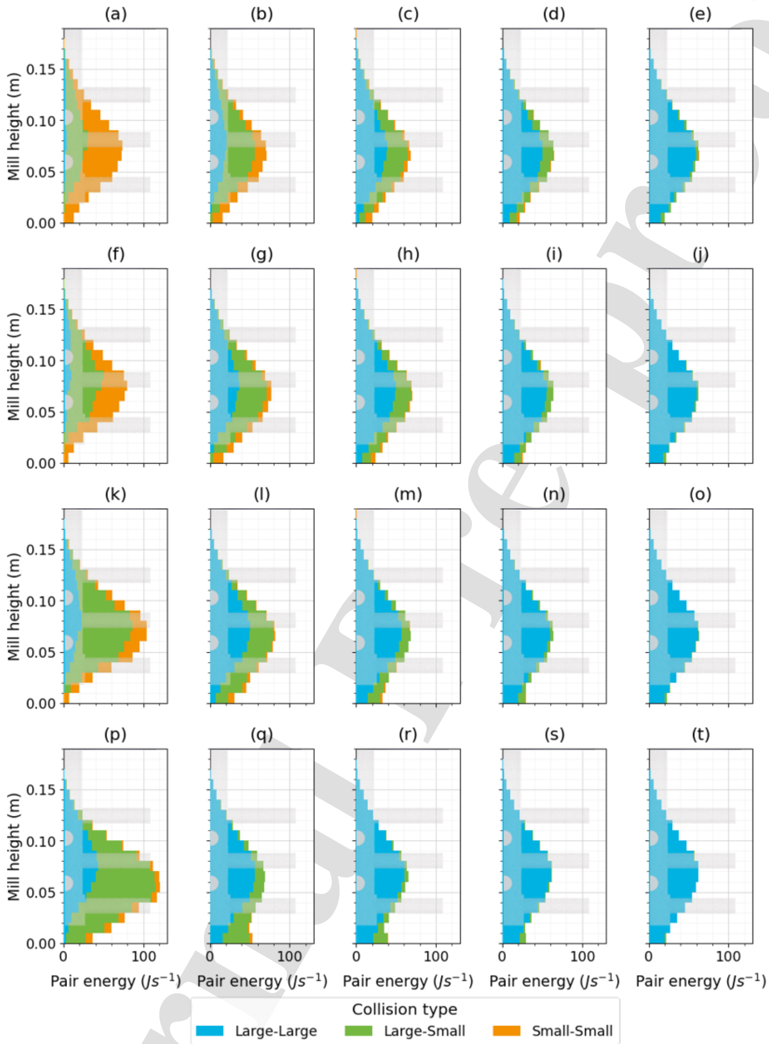

Figure 17: Pair stress energies by contact type at different heights of the mil, arranged by media diameter and proportionality. Left to right: 10 mm media at 10%, 30%, 50%, 70% and 90% proportionality. Top to bottom: smaller size of 7.5 mm, 6.25 mm, 5.0 mm and 3.75 mm. All plots are at 250 rpm.

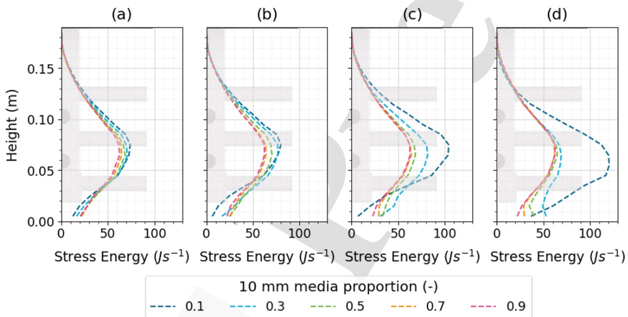

Figure 18: Distribution of pair stress energies per second by height for different proportionality at different media sizes. (a) 7.5 mm, (b) 6.25 mm, (c) 5.0 mm, and (d) 3.75 mm.

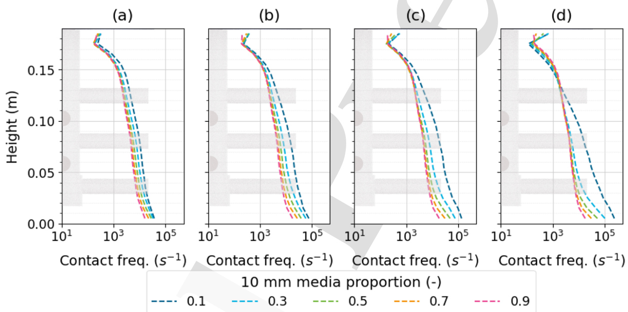

Figure 19: Contact frequency by height for different proportionality at different media sizes. (a) 7.5 mm, (b) 6.25 mm, (c) 5.0 mm, and (d) 3.75 mm.

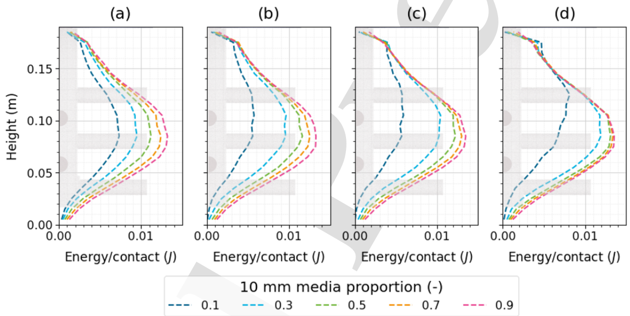

Figure 20: Energy per contact at different heights for different media sizes. (a) 7.5 mm, (b) 6.25 mm, (c) 5.0 mm, and (d) 3.75 mm.

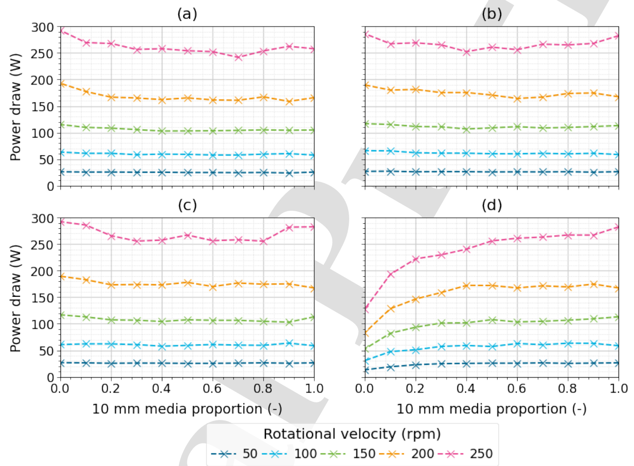

Figure 21: Calculated power draw for each simulation at different media ratios. (a) 7.5 mm, (b) 6.25 mm, (c) 5.0 mm, and (d) 3.75 mm.

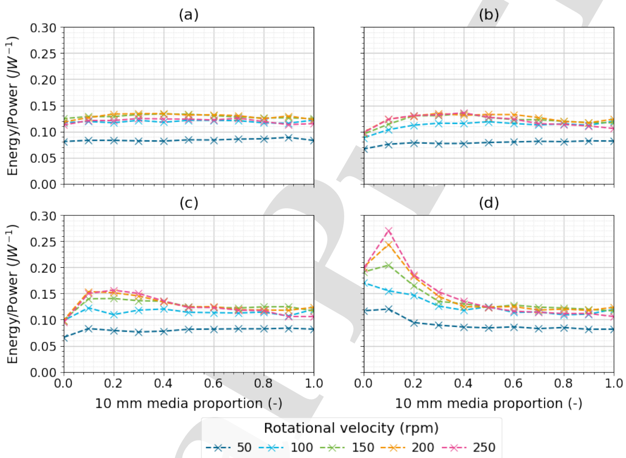

Figure 22: Efficiency plot of pair energy (Figure 15) divided by power draw (Figure 21) for each simulation. (a) 7.5 mm, (b) 6.25 mm, (c) 5.0 mm, and (d) 3.75 mm.

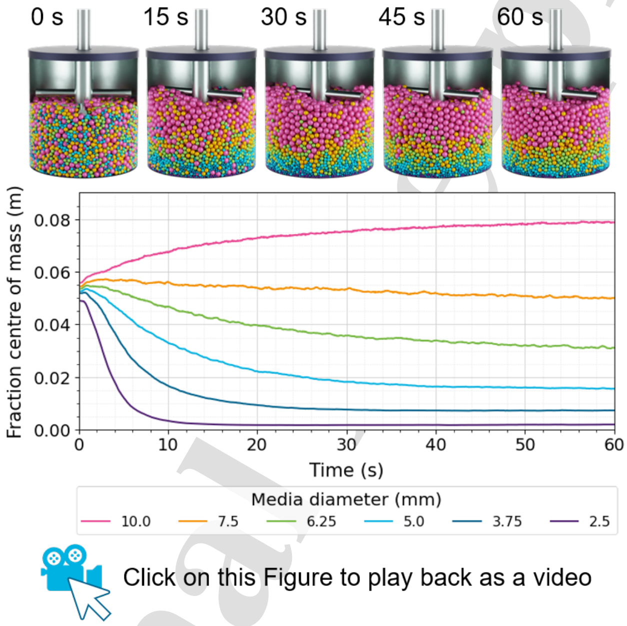

Figure 23: Image showing the progression of an equal count simulation of all six media diameters at different times, agitated at 50 rpm, with an additional plot showing the vertical centre of mass by media fraction.

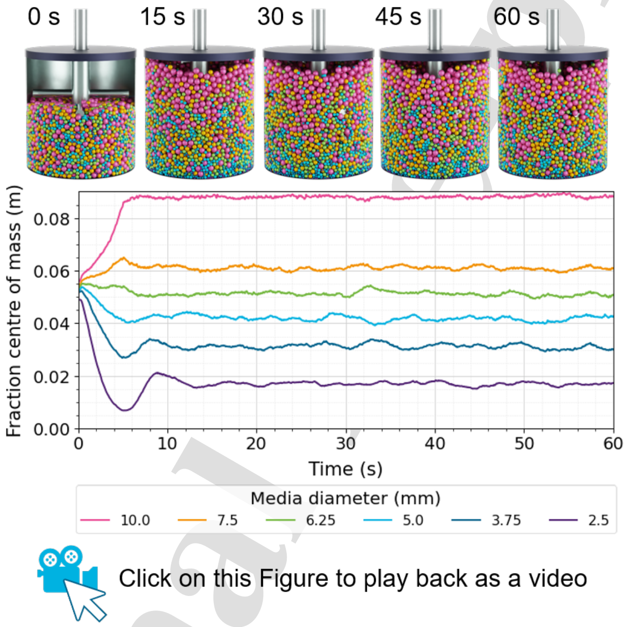

Figure 24: Images showing the progression of an equal count simulation of all six media diameters at 250 rpm for different times, with an additional plot showing the vertical centre of mass by media fraction.

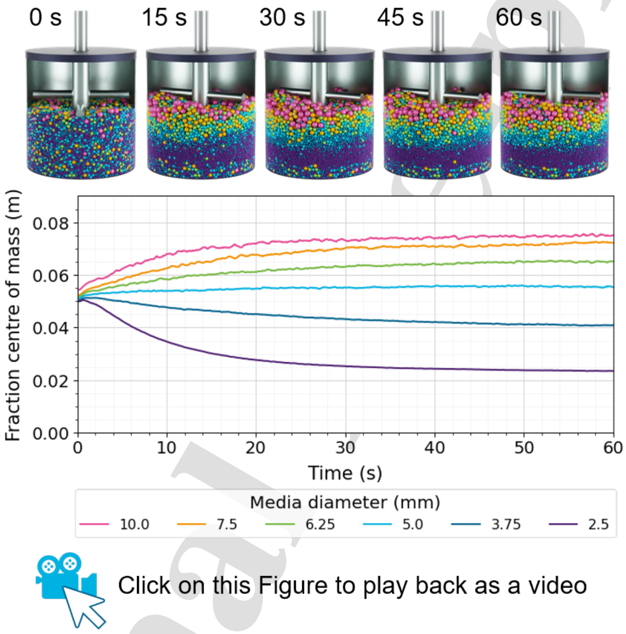

Figure 25: Images showing the progression of an equal volume simulation of all six media diameters at 50 rpm for different times, with an additional plot showing the vertical centre of mass by media fraction.

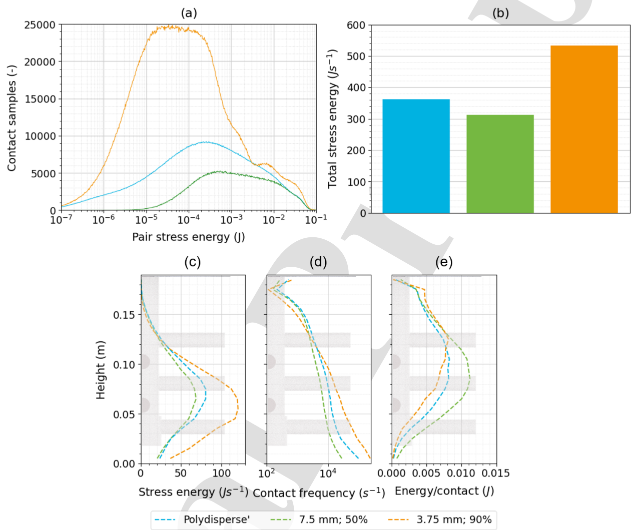

Figure 26: Energy and contact data comparing three scenarios: a polydisperse case by number, an equal count with a low size ratio, and a high proportion of small media with a high size ratio. (a) Logarithmic energy distribution per contact, (b) total stress energy per second, (c) energy distribution by height, (d) number of contacts across vessel height, and (e) energy per contact as a function of vessel height. All scenarios were run at 250 rpm.

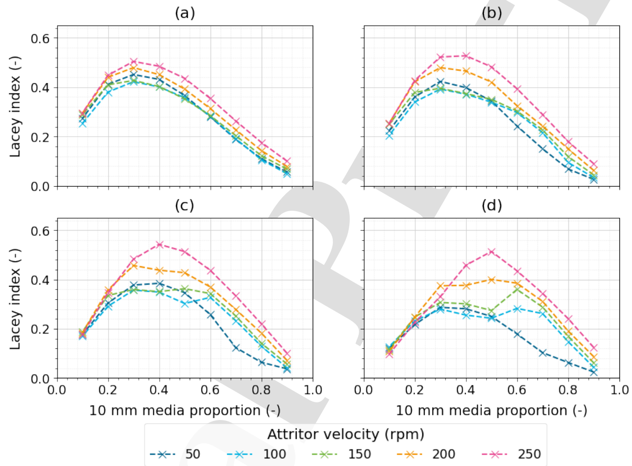

Figure 27: Calculated Lacey mixing indices for each simulation using $\varepsilon = 0.9$ and $\mu_s = 0.1$. (a) 7.5 mm, (b) 6.25 mm, (c) 5.0 mm, and (d) 3.75 mm.

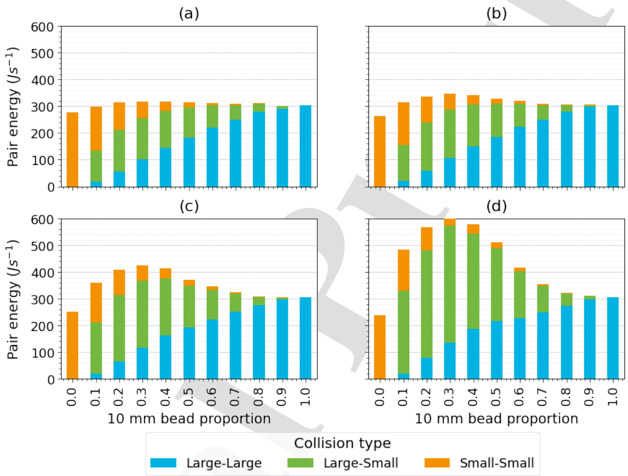

Figure 28: Overall collision energy spectra for different bead proportions and ratios at 250 rpm using $\varepsilon = 0.9$ and $\mu_s = 0.1$. (a) 7.5 mm, (b) 6.25 mm, (c) 5.0 mm and (d) 3.75 mm.

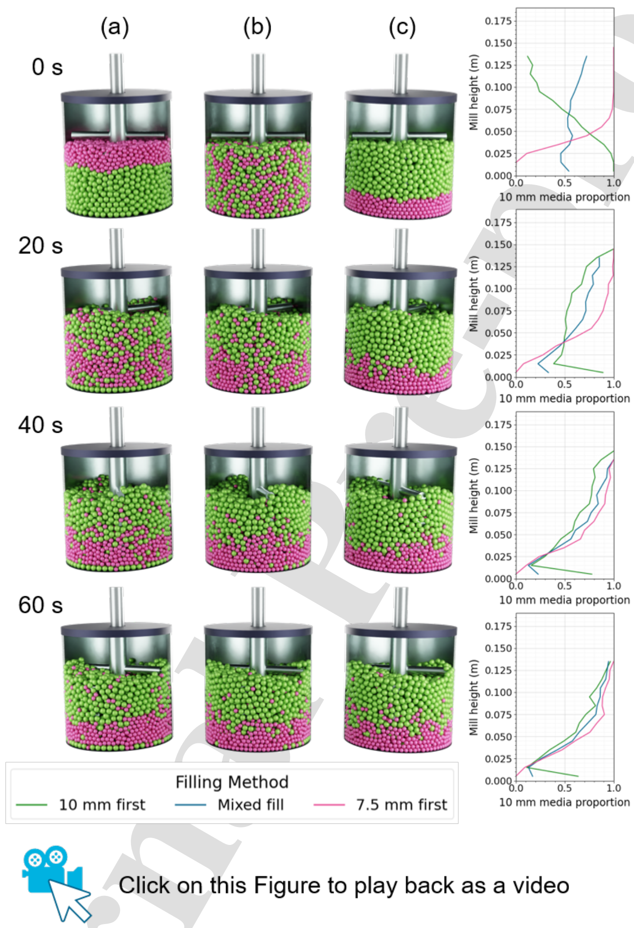

Figure 29: Progression of media motion over time, based on different starting fill conditions. All mills contain an equal number of 10 mm (green) and 7.5 mm (pink) media and were run at 50 rpm. (a) The large media are filled first, (b) the media are randomly filled, and (c) the small media are filled first. The plots on the right-hand side show the fraction of 10 mm media by mill height.

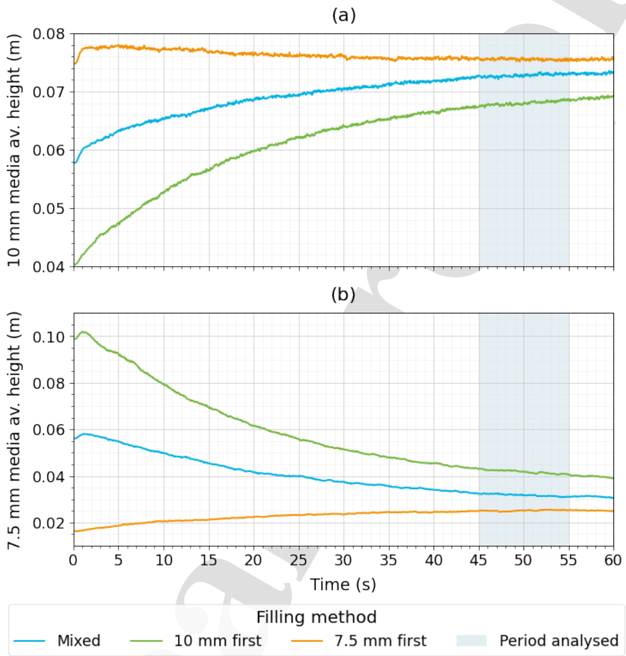

Figure 30: Progression of segregation over time after different starting fills using fraction centre of mass in the height axis. (a) 10 mm media, (b) 7.5 mm media. The shaded region between 45 and 55 seconds on each plot indicates the period analysed for all subsequent simulations.

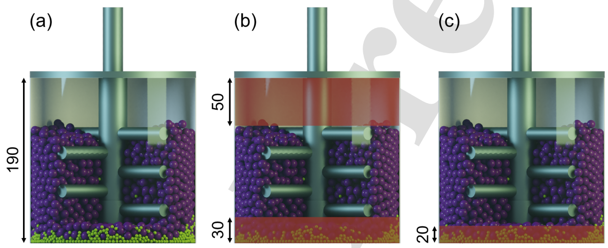

Figure 31: The different regions analysed within the mill, with red shading denoting the areas not analysed. All measurements are in mm. (a) Full mill region, (b) the area containing the pins, (c) removal of a noticeable dead zone below the impeller.

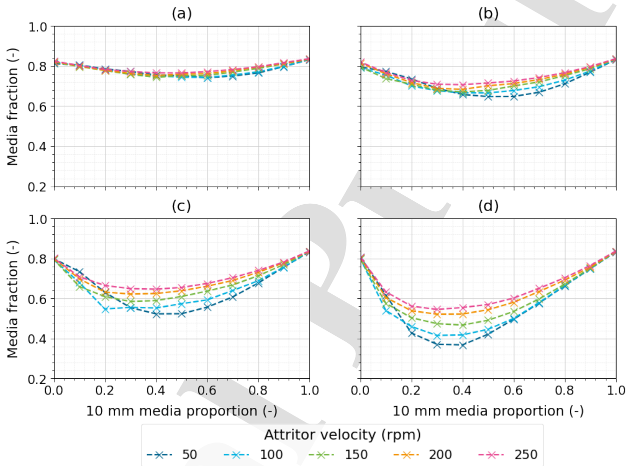

Figure 32: Fraction of all media by 10 mm bead proportion that are are above the bottom 20 mm of the milling space at different rotational velocities. (a) 7.5 mm, (b) 6.25 mm, (c) 5.0 mm, (d) 3.75 mm.

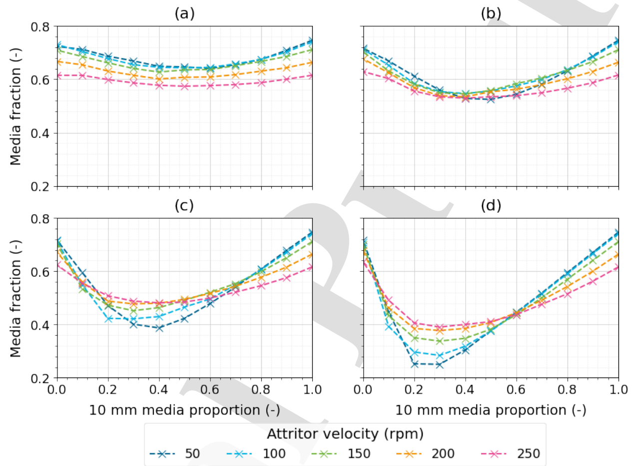

Figure 33: Fraction of all media that sit in-line with the attritor pins at different rotational velocities, plotted against the proportion of 10 mm media present. (a) 7.5 mm, (b) 6.25 mm, (c) 5.0 mm, (d) 3.75 mm.

Table 1: The six Equations defining contact pair collision mechanisms [52].

Mechanism	Symbol	Equation
Impact	E_{tn}	$E_{tn} = 0.5m(v_{ij}^{n})^2$
Torsion	E_{rn}	$E_{rn} = 0.2mR^2(\boldsymbol{\omega}_{ij}^{n})^2$
Shearing	E_{ts}	$E_{ts} = 0.5m(v_{ij}^{t})^2$
	E_{rs}	$E_{rs} = 0.2mR^2(\boldsymbol{\omega}_{ij}^{t})^2$
Rolling	E_{tr}	$E_{tr} = 0.5m(\boldsymbol{v}_i + \boldsymbol{v}_j)^2$
	E_{rr}	$E_{rr} = 0.2mR^2(\boldsymbol{\omega}_i + \boldsymbol{\omega}_j)^2$

Table 2: The fixed simulation parameters which were used for the investigation [36, 41]

Parameter	Value
Attritor rotational velocity range (rpm)	50-250
Large media diameter (mm)	10.0
Small media diameter range (mm)	2.5-7.5
Total media mass (kg)	14.80
Fill level (%)	55.0
Numerical proportion of large media (-)	0.0-1.0
Media density ($kg\,m^{-3}$)	7850
Young's Modulus ($N\,m^{-2}$)	2.1×10^7
Poisson ratio, ν (-)	0.3
Media-media restitution coefficient (-)	0.7
Media-media sliding friction (-)	0.3
Media-wall restitution coefficient (-)	0.7
Media-wall sliding friction (-)	0.3
Media rolling friction (-)	0.0
Timestep (s)	10^{-6}
Recorded simulation time (s)	10.0

Segregation in binary and polydisperse stirred media mills and its role on grinding effectiveness

D. Rhymer[1*], A. Ingram[1], K. Sadler[2] and C.R.K. Windows-Yule[1]
[1]School of Chemical Engineering, University of Birmingham, Edgbaston, B15 2TT
[2]R&D Mondelez International, Bournville, Birmingham, B30 2LU
[*]Corresponding author (dcr502@bham.ac.uk)

Paper Highlights

(Original)

- We investigate the effect of including multiple media sizes within a vertical mill.
- Changing size distribution can control the magnitude and frequency of media contacts.
- Power draw can be optimised, increasing the grinding sustainability.
- Natural segregation can be used to find ideal particle transport and flow patterns

(Revised)

- **We investigated the effect of including multiple media sizes within a vertical mill.**
- **Having two sizes can increase stress energy in the mill by up to 55%.**
- **Power draw can also be reduced by up to 30% by including a second size.**
- **Segregation means high-impact and high-attrition contacts occur simultaneously.**

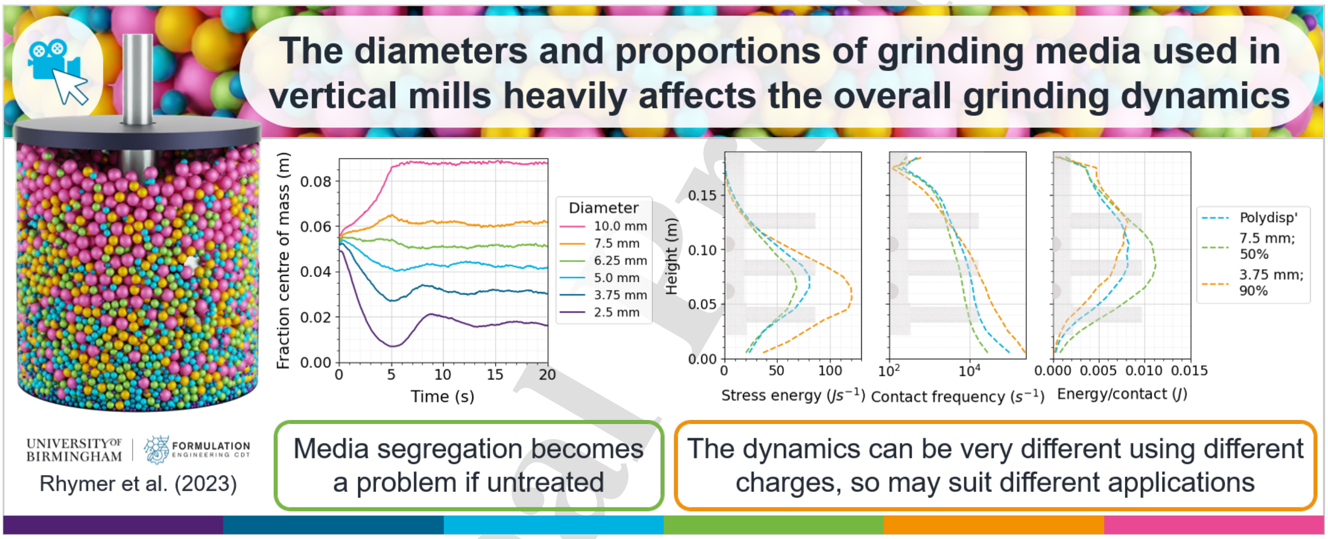
The diameters and proportions of grinding media used in vertical mills heavily affects the overall grinding dynamics
Fraction centre of mass (m)
0.08
0.06
0.04
0.02
0.00
0
5
10
15
20
Time (s)
Diameter
10.0 mm
7.5 mm
6.25 mm
5.0 mm
3.75 mm
2.5 mm
Height (m)
0.15
0.10
0.05
0.00
0
50
100
Stress energy (Js⁻¹)
10²
10⁴
Contact frequency (s⁻¹)
0.000
0.005
0.010
0.015
Energy/contact (J)
Polydisp'
7.5 mm; 50%
3.75 mm; 90%
UNIVERSITY OF BIRMINGHAM
FORMULATION ENGINEERING CDT
Rhymer et al. (2023)
Media segregation becomes a problem if untreated
The dynamics can be very different using different charges, so may suit different applications

Segregation in binary and polydisperse stirred media mills and its role on grinding effectiveness

D. Rhymer[1*], A. Ingram[1], K. Sadler[2] and C.R.K. Windows-Yule[1]

[1]School of Chemical Engineering, University of Birmingham, Edgbaston, B15 2TT
[2]R&D Mondelez International, Bournville, Birmingham, B30 2LU
[*]Corresponding author (dcr502@bham.ac.uk)

Credit Statement

Daniel Rhymer: Methodology, Model Development, Investigation, Data Curation, Data Analysis, Writing - Review & Editing.

Andy Ingram: Supervision, Data Analysis, Reviewing & Editing.

Kieran Sadler: Study Conceptualisation, Supervision.

Kit Windows-Yule: Supervision, Data Analysis, Reviewing & Editing.

Segregation in binary and polydisperse stirred media mills and its role on grinding effectiveness

D. Rhymer[1*], A. Ingram[1], K. Sadler[2] and C.R.K. Windows-Yule[1]
[1]School of Chemical Engineering, University of Birmingham, Edgbaston, B15 2TT
[2]R&D Mondelez International, Bournville, Birmingham, B30 2LU
[*]Corresponding author (dcr502@bham.ac.uk)

Declaration of Competing Interest

The authors declare upon submission that there are no competing interests.